Consistent Soil Moisture and Vegetation Optical Depth From Relatively Calibrated SMOS Brightness Temperatures With SMAP

Julian Chaubell, Simon H. Yueh, *Fellow, IEEE*, Andreas Colliander, Akiko Hayashi, Rajat Bindlish, *Senior Member, IEEE*, R. Scott Dunbar, Dara Entekhabi, *Fellow, IEEE*, Jun Asanuma, Aaron A. Berg, Alisa Coffin, Michael H. Cosh, *Senior Member, IEEE*, Gerald Flerchinger, Ann-Marie Fortuna, Chandra Holifield Collins, Taras Lychuk, José Martínez-Fernández, Kayla Moore, Zhongbo Su, and Jeffrey Walker

***Abstract*—The Soil Moisture Active Passive mission (SMAP, since 2015) from The National Aeronautics and Space Administration's (NASA) and Soil Moisture and Ocean Salinity mission (SMOS, since 2009) from The European Space Agency's (ESA) measure polarimetric brightness temperature (TB) at *L*-band (1.4 GHz). They provide estimates of surface soil moisture (SM) and *L*-band vegetation optical depth (L-VOD) approximately every 2–3 days at the equator, with a spatial resolution of ∼40 km for a local overpass time of 6 AM/PM. Integrating the AM and PM TB observations from SMAP and SMOS satellite missions can reduce the revisit time to about 1 day over the equator, thus helping to address fast-response hydrologic processes that cannot be addressed with the 2–3 day revisits. This will allow the capture of the SM conditions more often and, hence, capture the rate of decline due to drainage and recharge to groundwater. This occurs early during dry down after storms. The integration of SMOS measurements also works to fill temporal gaps caused by missing data due to SMAP instrument outages. This article details the integration of the SMAP and SMOS observations to achieve a combined SM and L-VOD product. The SMOS TB observations interpolated to 40° incidence angle were first relatively calibrated (RC) to generate SMAP-like SMOS TB (RCTB), making the combined TB records consistent spatially and temporally. The SMAP baseline SM and L-VOD retrieval algorithm was then applied to the RCTB records. We showed that after relative calibration (ARC), the bias between the SMAP and SMOS TBs was reduced from 0.5 to −0.03 K for TB H and from 2.6 to 0.014 K for TB V in the AM cases. For the PM cases, the mean value of differences was reduced from 0.82 to 0.27 K and from 2.88 to 0.19 K for TB H and TB V, respectively. The comparison of the core validation sites (CVS) in situ SM to the retrieved SM from the combined TB record showed an unbiased root-mean-square-difference of 0.039 m3/m3 for both AM and PM cases and the retrieved L-VOD demonstrated consistency with independent biomass and tree height estimates. We also showed an improvement in temporal coverage and that the global mean number of visits to each grid went up from 283 (SMAP only) to 446 (SMAP+SMOS) when both AM and PM overpasses are considered.**

***Index Terms*—Microwave radiometer intercomparison, passive microwave radiometry, soil moisture and ocean salinity mission (SMAP), SMOS, soil moisture (SM), vegetation optical depth.**

Received 23 September 2025; revised 30 December 2025 and 28 January 2026; accepted 13 February 2026. Date of publication 20 February 2026; date of current version 19 March 2026. The work was supported by the Jet Propulsion Laboratory, California Institute of Technology under a contract with the National Aeronautics and Space Administration. *(Corresponding author: Julian Chaubell.)*

Julian Chaubell, Simon H. Yueh, Akiko Hayashi, and R. Scott Dunbar are with the Jet Propulsion Laboratory, California Institute of Technology, Pasadena, CA 91109 USA (e-mail: julian@jpl.nasa.gov; simon.yueh@jpl.nasa.gov; akiko.k.hayashi@jpl.nasa.gov; roy.s.dunbar@jpl.nasa.gov).

Andreas Colliander was with the Jet Propulsion Laboratory, California Institute of Technology, Pasadena, CA 91109 USA. He is now with the Finnish Meteorological Institute, 00560 Helsinki, Finland (e-mail: andreas.colliander@fmi.fi).

Rajat Bindlish is with Goddard Space Flight Center, Greenbelt, MD 20771 USA (e-mail: rajat.bindlish@nasa.gov).

Dara Entekhabi is with the Massachusetts Institute of Technology, Cambridge, MA 02139 USA (e-mail: darae@mit.edu).

Jun Asanuma is with the Center for Research in Isotopes and Environmental Dynamics (CRiED), Tsukuba University, Tsukuba 305-8577, Japan (e-mail: asanuma@ied.tsukuba.ac.jp).

Aaron A. Berg is with the Department of Geography, Environment and Geomatics, University of Guelph, Guelph, ON N1G 2W1, Canada (e-mail: aberg@uoguelph.ca).

Alisa Coffin is with USDA-ARS Southeast Watershed Research, Tifton, GA 31793 USA (e-mail: alisa.coffin@usda.gov).

Michael H. Cosh is with USDA-ARS, Beltsville Agricultural Research Center, Hydrology and Remote Sensing Laboratory, Beltsville, MD 20705 USA (e-mail: michael.cosh@usda.gov).

Gerald Flerchinger is with USDA-ARS, Northwest Watershed Research Center, Boise, ID 83702 USA (e-mail: gerald.flerchinger@usda.gov).

Ann-Marie Fortuna is with USDA-ARS, Agroclimate and Hydraulic Engineering Research Unit, Stillwater, OK 74075 USA, and also with the Central Plains Agricultural Research Center, El Reno, OK 73036 USA (e-mail: ann–marie.fortuna@usda.gov).

Chandra Holifield Collins is with USDA-ARS, Oklahoma and Central Plains Agricultural Research CenteR, Agroclimate and Hydraulic Engineering Research Unit, El Reno, OK 73036 USA (e-mail: chandra.holifield@usda.gov).

Taras Lychuk and Kayla Moore are with Agriculture and Agri-Food Canada (AAFC), Brandon, MB R7A 5Y3, Canada (e-mail: taras.lychuk@agr.gc.ca; kayla.moore@agr.gc.ca).

José Martínez-Fernández is with Instituto Hispano Luso de Investigaciones Agrarias (CIALE), Universidad de Salamanca, 37008 Salamanca, Spain (e-mail: jmf@usal.es).

Zhongbo Su is with the ITC Faculty, University of Twente, 7522 NB Enschede, The Netherlands (e-mail: z.su@utwente.nl).

Jeffrey Walker is with Monash University, Clayton, VIC 3800, Australia (e-mail: jeff.walker@monash.edu.au).

Digital Object Identifier 10.1109/JSTARS.2026.3666810

I. Introduction

THE National Aeronautics and Space Administration's (NASA) Soil Moisture Active Passive (SMAP, since 2015) and European Space Agency's (ESA) Soil Moisture and Ocean

Salinity (SMOS, since 2009) missions measure *L*-band (1.4 GHz) brightness temperature (TB) and provide estimates of surface soil moisture (SM) and *L*-band vegetation optical depth (L-VOD) [1], [2], [3], [4]. The SMAP 1.4 GHz *L*-band radiometer measures vertical (V) and horizontal (H) polarized TBs and the third and fourth Stokes parameters. It provides a constant native 38-km resolution sampled from a 6 AM/PM equatorial crossing sun-synchronous orbit. The 1000-km swath width, resulted from the conically scanning at 40° incidence angle, allows for a 2–3 day equatorial revisit time [5], [6]. Similarly, SMOS Microwave Imaging Radiometer using Aperture Synthesis (MIRAS instrument), which is an *L*-band interferometric aperture synthesis radiometer, observes the Earth with multiple incidence angles ranging from 0° to 55° [7], [8]. At each incidence angle, MIRAS measures the V and H polarization and the third and fourth Stokes parameters with a footprint size varying from 35 to 50 km, depending on the incidence angle (the larger the incidence angle, the larger the footprint) [9]. The image processing can include or exclude the so-called extended alias-free field-of- view (FOV), affecting the swath width, with the extended alias-free FOV having a swath of 1300 km, while the alias-free FOV has a swath of 630 km (e.g., [10]). The extended alias-free region has larger errors due to the residuals remaining from the imperfect aliasing corrections; studies have found that excluding the extended alias-free FOV can provide improved SM and L-VOD retrieval performance (e.g., [11], [12]). However, the reduction of the swath width leads to longer revisit times.

Integrating the SMAP (AM/PM) and the SMOS (AM/PM) TB observations can reduce the revisit time to about 1 day, thus allowing the monitoring of fast-response processes that cannot be addressed with a 2–3-day revisit. This will enhance the capture of rapid SM declines due to drainage following precipitation events. Following precipitation events, the wet SM declines more rapidly due to its higher hydraulic conductivity (e.g., [13], [14], [15]). For sufficiently wet soil, rapid drainage under gravity reduces the SM to its field capacity in short periods of time (typically hours to one to two days). Combined SMAP and SMOS data with both ascending and descending overpasses provides greater opportunity to capture such SM dynamics in the period after precipitation events. Another benefit of such integration is that it will allow us to fill data gaps caused by failures in the SMAP radiometer instrument such as occurred in 2019 between June 20th and July 22nd.

The performance of the SM and L-VOD products of each mission has been evaluated in numerous studies, mainly indicating consistent performance between them. The somewhat higher noise in the SMOS extended alias-free FOV and the susceptibility of SMOS to radio-frequency interference (RFI) (e.g., [16]) in contrast to the dedicated RFI filtering features of SMAP ([17]; [18]), have, however, created some differences (e.g., [19], [20], [21], [22], [23]). The multiangle measurements of SMOS provide an advantage for more independent L-VOD determination (e.g., [3]). These results generally point to a relatively straightforward combination of the products from the two missions. Still, due to the different instrument configurations, ancillary data, retrieval algorithms, and calibration strategies of SMAP and SMOS, developing an integrated TB, SM, and L-VOD data product is not practical through a simple merging of the corresponding products. Previous efforts to integrate the SMOS and SMAP TB observations have been presented by others [24], [25], [26]. Bindlish et al. [24] presented preliminary studies to merge the SMAP L1B product (36 km resolution) and SMOS TBs measurements fitted at 40° incidence angle to obtain an integrated SM product using the SMAP single channel retrieval algorithm. This study planted the seed for the work presented in this article to generate an enhanced SM and VOD product (9 km posting resolution) by using the double channel algorithm (DCA), which is today the SMAP baseline retrieval algorithm. In [25], an effort to merge the SMOS TB and SMAP TB is described. The authors used the *L*-band microwave emission of the biosphere model to fit the SMOS TB dataset at a fixed incidence angle of 40°, and then a monthly linear rescaling of the SMAP TB to the SMOS TB was applied to each polarization to reduce the SMOS-SMAP TB mean difference (MD). It is important to notice that the SMAP TB at 9 km posting resolution was resampled to match the 25 km SMOS grid spatial resolution. The retrieval of SM and L-VOD was then performed using the SMOS-IC algorithm, SMOS ancillary data, SMOS TB and SMOS-like SMAP TBs (RC SMAP TB to SMOS), resulting in an integrated product called SMOSSMAP-INRAE-BORDEAUX. SMOSSMAP-IB provides three products: SMOS/SMAP integrated TBs, SM, and VOD at a 25 km grid spatial resolution. Paţilea et al. [26] used data from both sensors to obtain a combined sea ice thickness dataset by intercalibrating the SMAP TBs to the SMOS TBs, thus improving the temporal and spatial coverage of the polar regions.

A consistent integration of data from both missions requires the following:

1) processing of the SMOS TB to match the SMAP fixed 40° incidence angle;
2) a relative calibration (RC) between the SMOS and SMAP TB generating the SMAP-like SMOS TBs (or relative calibrated TB (RCTB);
3) elimination of the water contamination in the SMOS TB over land;
4) processing of the SMAP ancillary data over the 9 km EASE-Grid V2.0 at the SMOS overpass time;
5) application of the SMAP retrieval algorithm to the processed RCTB to obtain SM and L-VOD.

This article details integrating the SMAP and SMOS observations, to achieve a combined TB SM and L-VOD products over the 9 km EASE2 grid, consistent with the SMAP enhanced products posting resolution. This article contains the following sections: Section II describes the methodology utilized to integrate both products. In Section II-A, the procedure to compute the SMOS TB at the fixed 40° incidence angle is described. In Section II-B, the methodology for RC between the missions' TBs is detailed. In Section II-C, the algorithm to correct the TB for water contamination is introduced. In Section II-D, the SMAP dual channel algorithm (DCA) to obtain SM and L-VOD is reviewed and the selection of ancillary data is described. In Section III, the different steps of the algorithms are evaluated and in Section IV, the performance assessment of SM and VOD

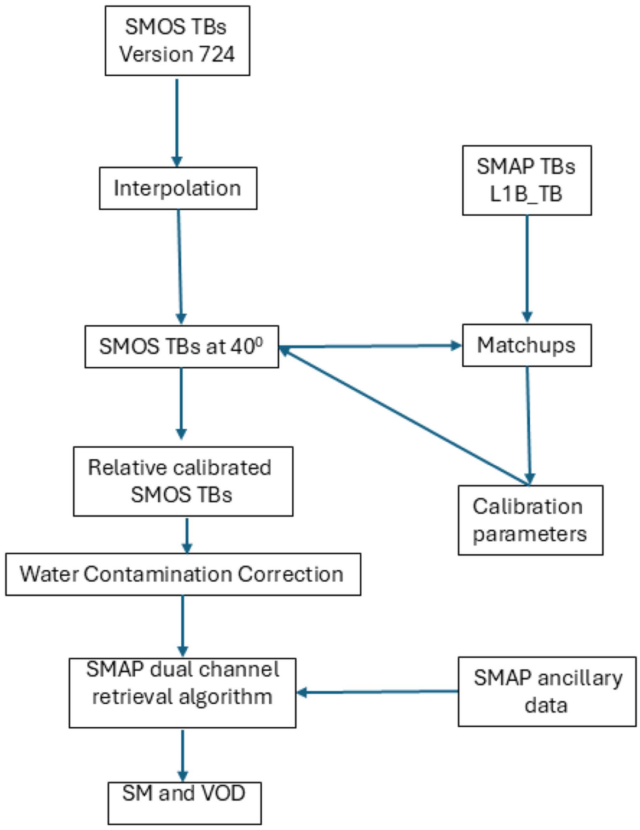

Fig. 1. Algorithm flow.

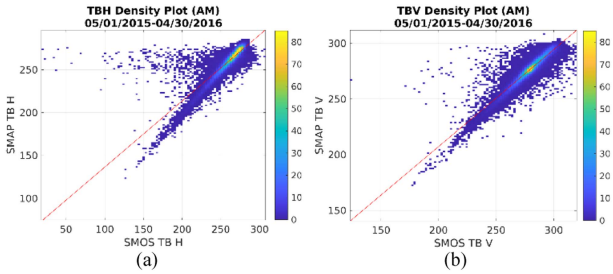

Fig. 2. Density plot of the L1 TB comparison between SMAP and SMOS (interpolated to the incidence angle of 40°) over land targets for V-pol (right) and H-pol (left). No RFI filtering was applied.

retrieval is presented. Finally, Section V provides discussion and summary.

II. Methodology

To obtain SMAP-like SM and VOD based on RC SMOS TB, the following steps were taken:

1) the SMOS-based TB at 40° incidence angle were RC to SMAP, as detailed in Sections II-A and II-B;
2) the TBs were corrected for water contamination as explained in Section II-C;
3) the DCA retrieval algorithm was finally applied using the ancillary data obtained directly from the SMAP L2_SM_P_E as detailed in Section II-D.

Fig. 1 summarizes the algorithm flow.

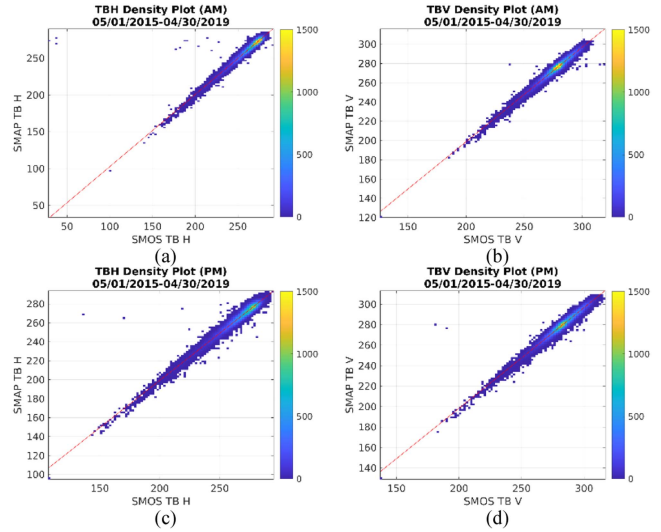

Fig. 3. Density plot of the L1 TB comparison between SMAP and SMOS observations over land targets for H-pol [(a) and (c)] and V-pol [(b) and (d)] after the RFI filtering was applied. Top row: AM half orbits. Bottom row: PM half orbits.

A. SMOS TB at 40° Incidence Angle

To process the SMOS L1C TB to the constant 40° incidence angle a multistep regression and curve fitting approach was used [27]. The L1C SMOS product contains TB at different angles in the antenna frame (*X*–*Y*) at the top of the atmosphere for each fixed SMOS discrete global grid and different SMOS snapshots. These observations need, first, to be converted into vertical (V) and horizontal (H) polarized components referenced to the Earth's surface. This conversion considers the rotation of the electric fields due to the geometrical orientation difference between the antenna reference frame and the Earth's surface and the Faraday rotation induced by the effect of ionospheric electrons on the propagation of electromagnetic waves. To perform the transformation, all four Stokes parameters are needed. Since not all the Stokes parameters are provided within a single SMOS snapshot, a time-series interpolation is applied to supplement the complete set of observations. Once the complete set of Stokes parameters is obtained for each snapshot, the *X* and *Y* polarized TB (antenna level) are transformed to *H* and *V* polarized TB using

$$\begin{bmatrix} TB_h \\ TB_v \\ T_3 \\ T_4 \end{bmatrix} = R^{-1} \begin{bmatrix} A_1 \\ A_2 \\ A_3 \\ A_4 \end{bmatrix} \tag{1}$$

where $A_1 = \text{real}(T_{xx})$, $A_2 = \text{real}(T_{YY})$, $A_3 = 2\,\text{real}(T_{xy})$, $A_4 = -2\,\text{imag}(T_{xy})$, with T_{xx}, T_{yy}, and T_{xy} the co-pol and cross-pol SMOS measurement, respectively. The rotation matrix *R* is given by

$$R = \begin{bmatrix} cos^2\alpha & sin^2 & -\cos\alpha\sin\alpha & 0 \\ \sin\alpha^2 & \cos\alpha^2 & \cos\alpha\sin\alpha & 0 \\ \sin 2\alpha & -\sin 2\alpha & \cos 2\alpha & 0 \\ 0 & 0 & 0 & 1 \end{bmatrix} \tag{2}$$

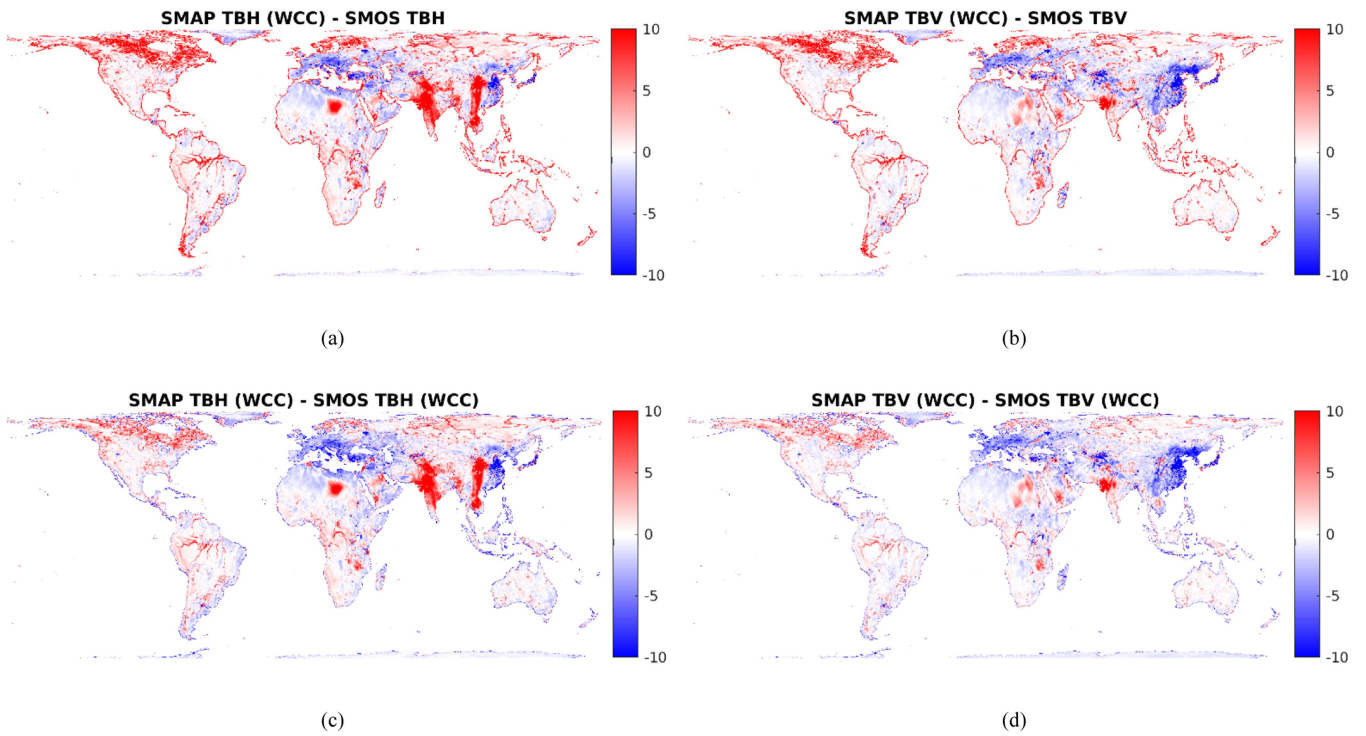

Fig. 4. Global maps of TBs differences after and before RC SMOS TBs were corrected for water contamination. Top row: SMAP WCC TBH and TBV minus RC SMOS TBV and TBH before WCC. Bottom row: SMAP WCC TBH and TBV minus RC SMOS TBV and TBH after water contamination correction.

where α is the rotation angle $\alpha = \text{Fa} + \text{Ga}$ with Fa and Ga, the Faraday rotation angle and the angle representing the geometrical orientation difference between the antenna reference frame and the Earth's surface, respectively.

The multiangular observations at the Earth's surface level are then used to obtain, by interpolation, the TB at the SMAP 40° incidence angle following [27].

B. Calibration Parameters and TB Intercalibration

The SMOS and SMAP missions rely on two different instrument configurations. They use a different set of ancillary data, different retrieval algorithms, and different calibration strategies, making it challenging to develop an integrated TB, SM, and VOD data product through a simple combination of their products. Successful integration of observations from both missions requires the removal of the systematic MDs between the SMOS and SMAP TB, among other factors. To remove the MD between the two sets of data, we performed an intercomparison between them and computed a linear regression of SMAP TB versus SMOS TB, providing us with the RC parameters (slope and offset). Footprints TB measurements from each mission separated by less than 1 km at the surface were used in the intercomparison. The comparisons were made after the measured TB were corrected for reflected galaxy, ionosphere, and atmospheric effects. To minimize intercomparison errors associated with temporal changes in SM and temperature, a maximum time window between the two satellite observations of 30 min was used. Quality flags from both missions were used in the analysis. Only TB observations with the quality flags indicating no anomalies were used in the matchups. The data were also filtered by the RFI probability information included in the SMOS data files. Only footprints with the RFI probability equal to zero were considered. This analysis was undertaken for both H and V polarizations over land only. To minimize the error caused by water contamination, only TB values over grid cells with water fractions less than 0.01 were compared. The analysis used the SMAP data product L1B_TB version 6 and SMOS L1C data product version 724.

Fig. 2 shows density plots of the TB comparisons between SMAP and SMOS TBs over land for V and H polarizations before applying the RFI filter. Those plots show a relatively weak correlation. The data appear very noisy, with a substantial difference between the high values of the SMAP TB and the low values of the SMOS TB. The linear regression shows slope values of 0.87 and 0.77 for the V-pol and H-pol, respectively, and offsets of 59.43 K for V and 33.2 K for H. The cause of the observed noise could be attributed to the presence of RFI in the data. Fig. 3 displays density plots of the SMAP TB versus the SMOS TB for AM and PM passes, covering a time range from 1 May 2015 to 30 April 2019 after the SMOS measurements were filtered for RFI (a threshold of zero for the SMOS RFI probability was used). The plots show cleaner density plots, an indication that RFI was, indeed, the source of the noise. Table I shows the computed correlation parameters after excluding the outliers in Fig. 3; these parameters were used to relative calibrate the SMOS TB with the SMAP TB. The RC was applied to each SMOS orbit pass after the SMOS TBs were collocated over the

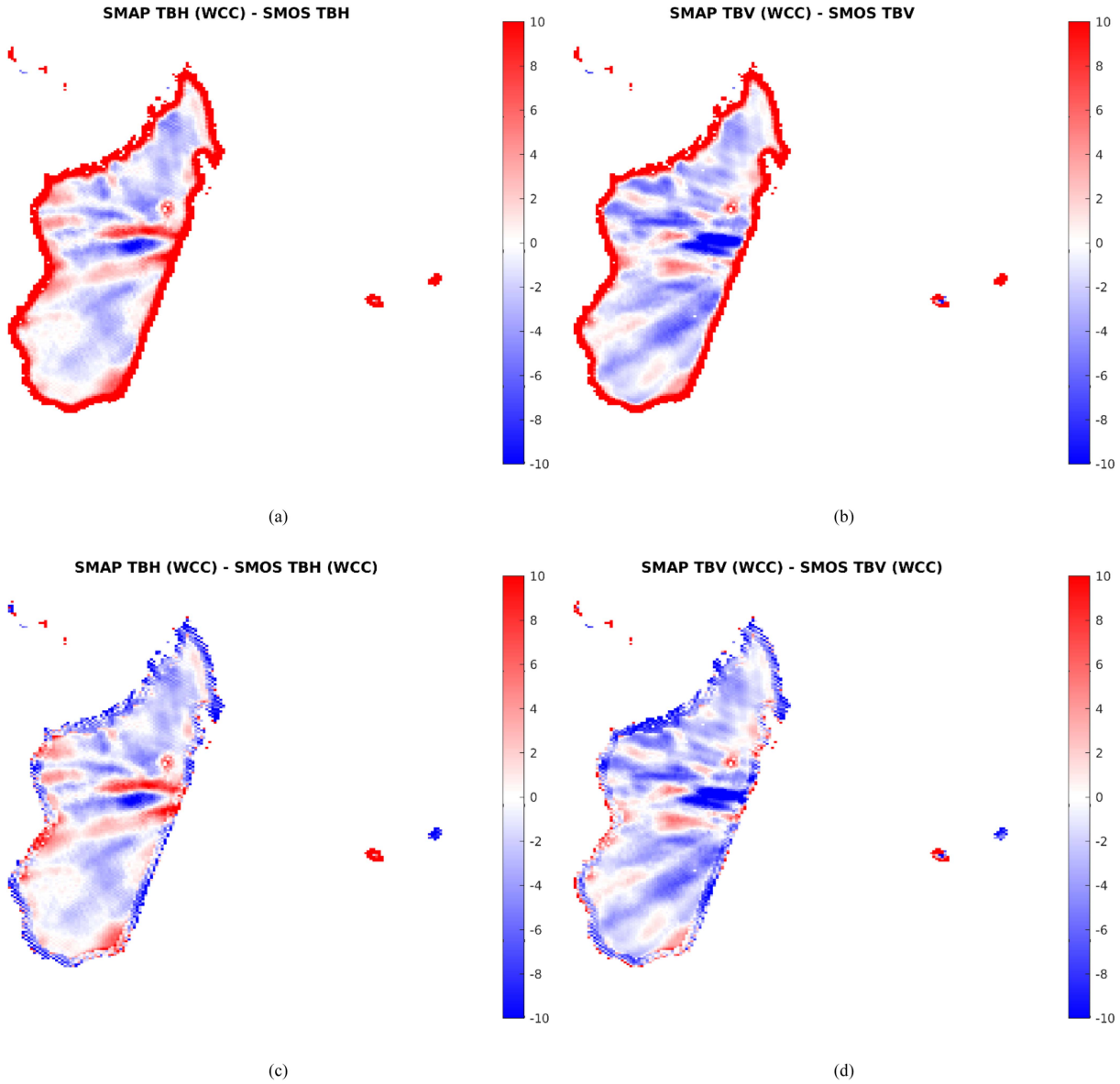

Fig. 5. Zoom of images on Fig. 3 over Madagascar. (a) and (b): SMAP WCC TBH and TBV minus RC SMOS TBH and TBV before correction. (c) and (d): SMAP WCC TBH and TBV minus RC SMOS TBH and TBV after correction.

TABLE I
INTERCALIBRATION PARAMETERS

	TB-H (AM)	TB-H (PM)	TB-V (AM)	TB-V (PM)
Slope	0.9967	0.9989	0.9827	0.9878
Offset	0.3310	−0.5246	2.204	0.5679

9 km SMAP grid. Evaluation of differences between SMOS and SMAP TBs, before and after RC, showed that the MDs were reduced from 0.5 to −0.03 K for TB H and from 2.6 to 0.014 K for TB V in the AM cases. For the PM cases, the mean values of differences were reduced from 0.82 to 0.27 K and from 2.88 to 0.19 K for TB H and TB V, respectively.

C. *Water Contamination Correction*

For land pixel close to water bodies, the correction of the SMOS TB by eliminating the water contribution to the measurement is needed before the retrieval of SM. The resulting TB becomes warmer upon the removal of the water contribution than the original TB. Following the SMAP water contamination removal algorithm [28], the correction is performed if the antenna-gain-weighted water fraction within the grid cell is less than or equal to 0.9 (water fraction equals one indicates pure water) and when the grid cell center falls on a land location based on a static high-resolution land/water mask. The correction is not applied when ice fraction is greater than zero. The correction of the SMOS water-contaminated TB over coastal areas and around inland water bodies used the same algorithm as the

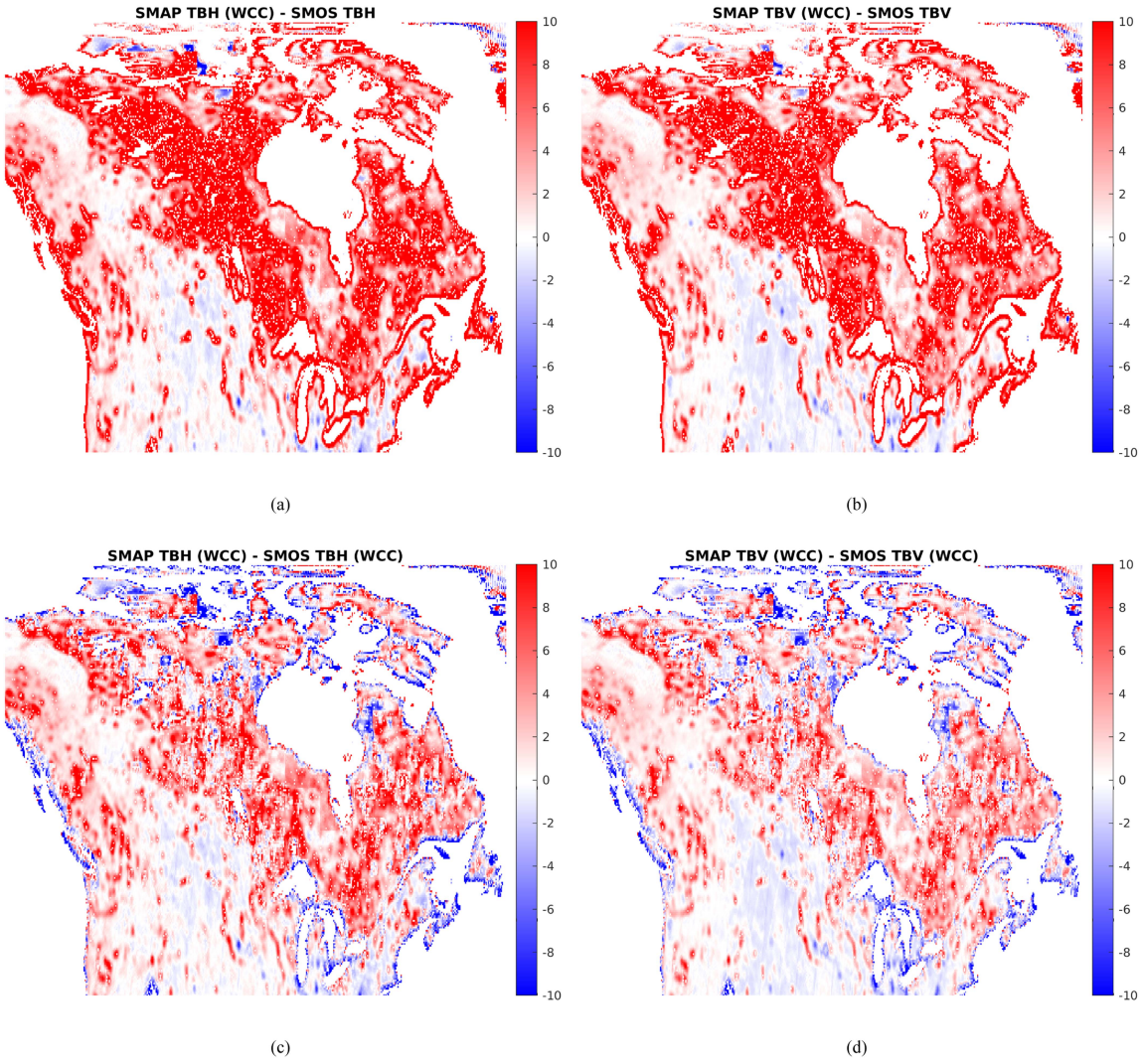

Fig. 6. Zoom of images on Fig. 3 over the Great Lakes and Canada. (a) and (b): SMAP WCC TBH and TBV minus RC SMOS TBH and TBB before correction. (c) and (d): SMAP WCC TBH and TBV minus RC SMOS TBH and TBV after correction.

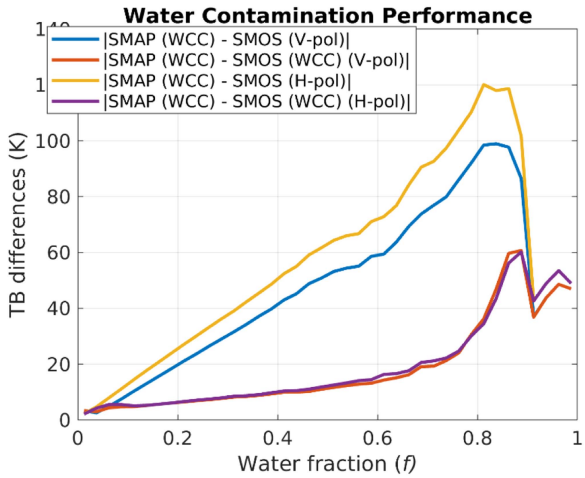

Fig. 7. Averaged absolute TB differences as a function of water fraction. It compares SMAP TB with the water body correction—SMOS TB with and without the water body correction.

SMAP processing [28]

$$T_B^{\text{land}} = \frac{T_B - f\hat{T}_B^{\text{water}}}{1-f} \tag{3}$$

where f accounts for the water fraction and $\hat{T}_B^{\text{water}}$ is the expected water body TB around the grid cell under consideration.

As shown in (3), to correct the SMOS TB, the water fractions for each grid center are needed, as well as the TB expected from ocean and inland water bodies affecting the observed TB. The available SMAP product was used to obtain those parameters. Eight years of SMAP data from the L1C_TB_E SMAP product were used to compute the average water fraction (V and H polarizations) and water body TB (V and H polarizations) for each global 9 km grid node, thus generating climatology global maps of the desired parameters.

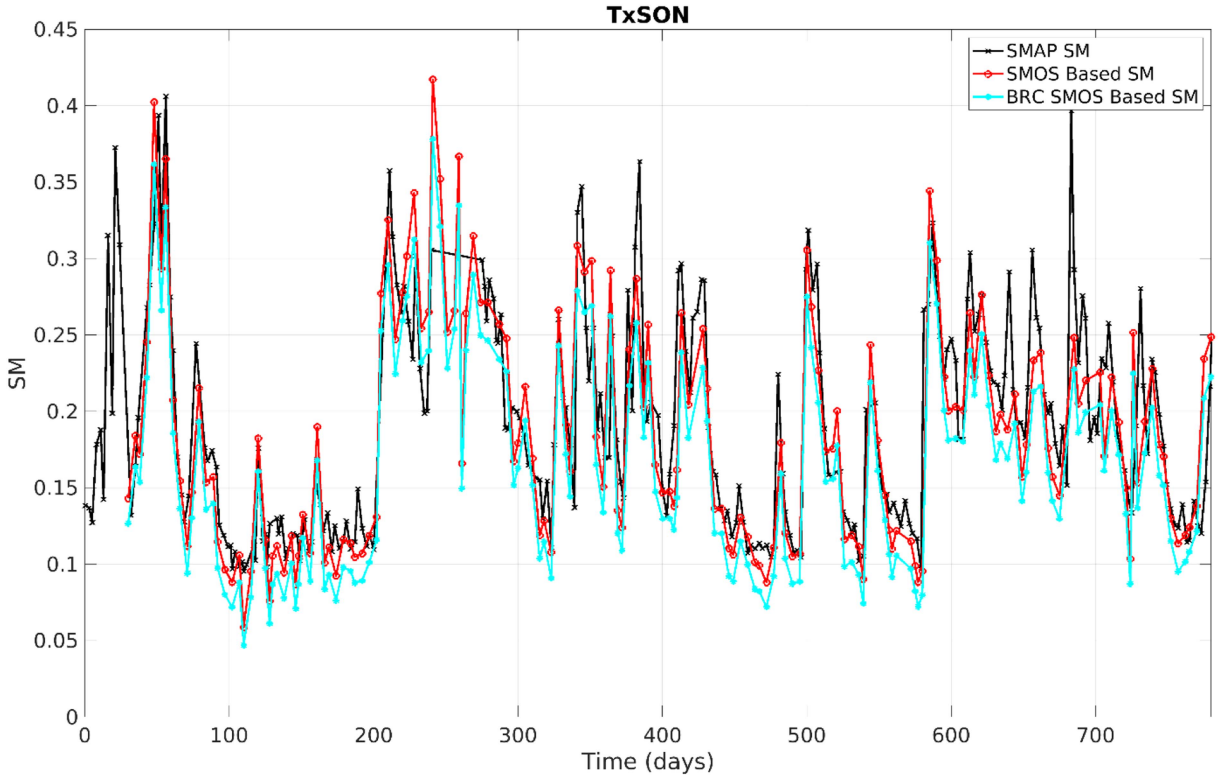

(a)

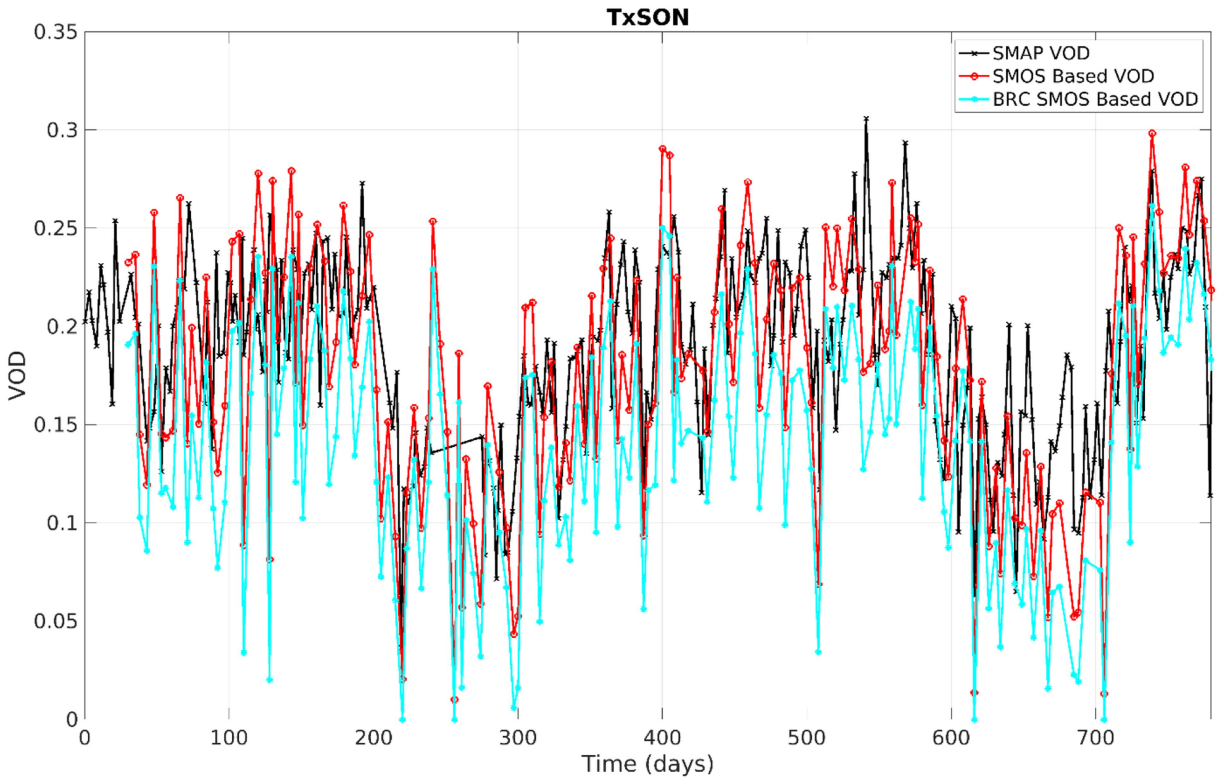

(b)

Fig. 8. Time series of SM (top) and VOD (bottom) over TxSON (CVS). SMAP data in black. SMOS-based before relative calibration (BRC) in red and SMOS-based after relative calibration (RC) in cyan.

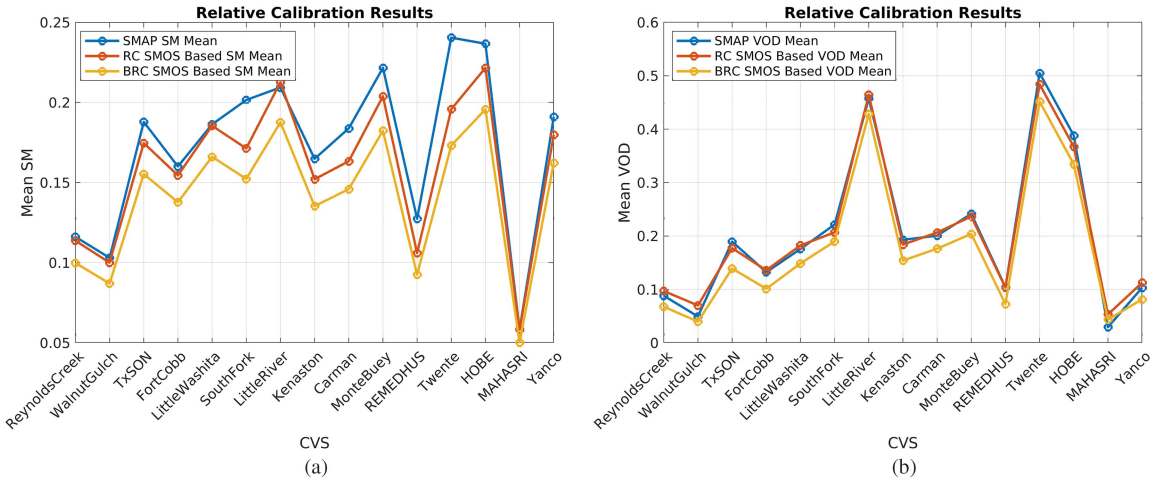

Fig. 9. (a) Mean values of SM and (b) mean values of VOD over the CVS time series as displayed for TxSON on Fig. 8.

D. Retrieval Algorithm

To retrieve SM and VOD from the SMOS-based TB at 40° incidence angle, the SMAP baseline SM retrieval algorithm (DCA), based on the approximation of the radiative transfer equation known as the Tau-Omega model, was used. The DCA, which uses both H-pol and V-pol TB, retrieves SM and VOD by minimizing the cost function (4) [28]

$$F\ (\mathrm{sm}, \tau) = \left(\mathrm{TB}_V^{\mathrm{obs}} - \mathrm{TB}_V^{\mathrm{modeled}}\right)^2 + \left(\mathrm{TB}_H^{\mathrm{obs}} - \mathrm{TB}_H^{\mathrm{modeled}}\right)^2 + \lambda^2(\tau - \tau^*)^2 \quad (4)$$

where $\mathrm{TB}_V^{\mathrm{modeled}}$ and $\mathrm{TB}_H^{\mathrm{modeled}}$ are the TB modeled by the Tau-Omega model, $\mathrm{TB}_V^{\mathrm{obs}}$ and $\mathrm{TB}_H^{\mathrm{obs}}$ are the SMAP measurements, λ is a regularization parameter, and τ^* is the vegetation optical depth initial guess.

The DCA implementation [29], requires the a priori determination of several parameters: the effective surface temperature, which is a dynamic parameter and the static parameters, including clay fraction, bulk fraction, roughness coefficient, single scattering albedo (ω), and the VOD based on normalized difference vegetation index (NDVI) τ. The abovementioned parameters were obtained directly from the SMAP_L2_SM_P_E product instead of using the direct input from the SMAP ancillary files to mimic the SMAP algorithm as closely as possible. The SMAP processing algorithm applies a 33-km spatial averaging window over the ancillary data (see [30, Fig. 3]), and so, using the data directly from the ancillary files would lead to some differences in the retrievals. Eight years of data (1 April 2015–31 March2023) were used to generate climatology maps of those parameters over the EASE-Grid V2.0 global projection system. In the case of the NDVI τ, day-of-the-year climatology global maps were obtained. For the effective surface temperature (dynamic parameter), the data were taken directly from the GMAO ancillary files at the SMOS overpass time.

III. Algorithm Evaluation

A. Water Contamination Correction Evaluation

Fig. 4 compares the SMAP TBs corrected for water contamination against the SMOS TBs before and after water contamination correction was applied. The relative-calibrated (RC) SMOS TBs were not filtered for RFI. On the top row [see (a) and (b)], the figure displays the water body corrected SMAP TBH and TBV minus the RC SMOS TBH and TBV without the water body correction. On the bottom row [see (c) and (d)], the figure displays the corrected SMAP TBH and TBV minus the RC SMOS TBH and TBV with the water body correction applied. In the panels at the top, the red around inland water bodies and along coastal areas indicates differences greater than 10 K between the corrected SMAP TBs and the uncorrected SMOS TBs. On the panels at the bottom, the borders around water bodies were reduced or disappeared, indicating the success of the correction algorithm. Fig. 5 displays a zoom of the Fig. 4 images over Madagascar, clearly showing the success of the water correction algorithm over the area. Fig. 6 displays a zoom of the Fig. 4 images over the Great Lakes and Canada showing areas where some residual contamination remains even though the contamination was reduced. These residuals could be in either SMAP, SMOS, or both datasets and due to the fact that we do not apply the algorithm in the presence of ice. Fig. 7 shows averaged absolute TB differences as a function of water fraction comparing SMAP TB with the correction—RC SMOS TB with and without the correction. The differences were improved by between 15 and 70 K for the 0.2–0.8 water fraction range for the V-pol, and between 15 and 90 K for the H-pol.

B. Impact of TB RC on SM Retrieval

To evaluate the effect of the RC over the retrieved SM and VOD, the time series of those parameters were examined over the core validation site (CVS) before and after the calibration was applied. Fig. 8 compares the time series over the TxSON

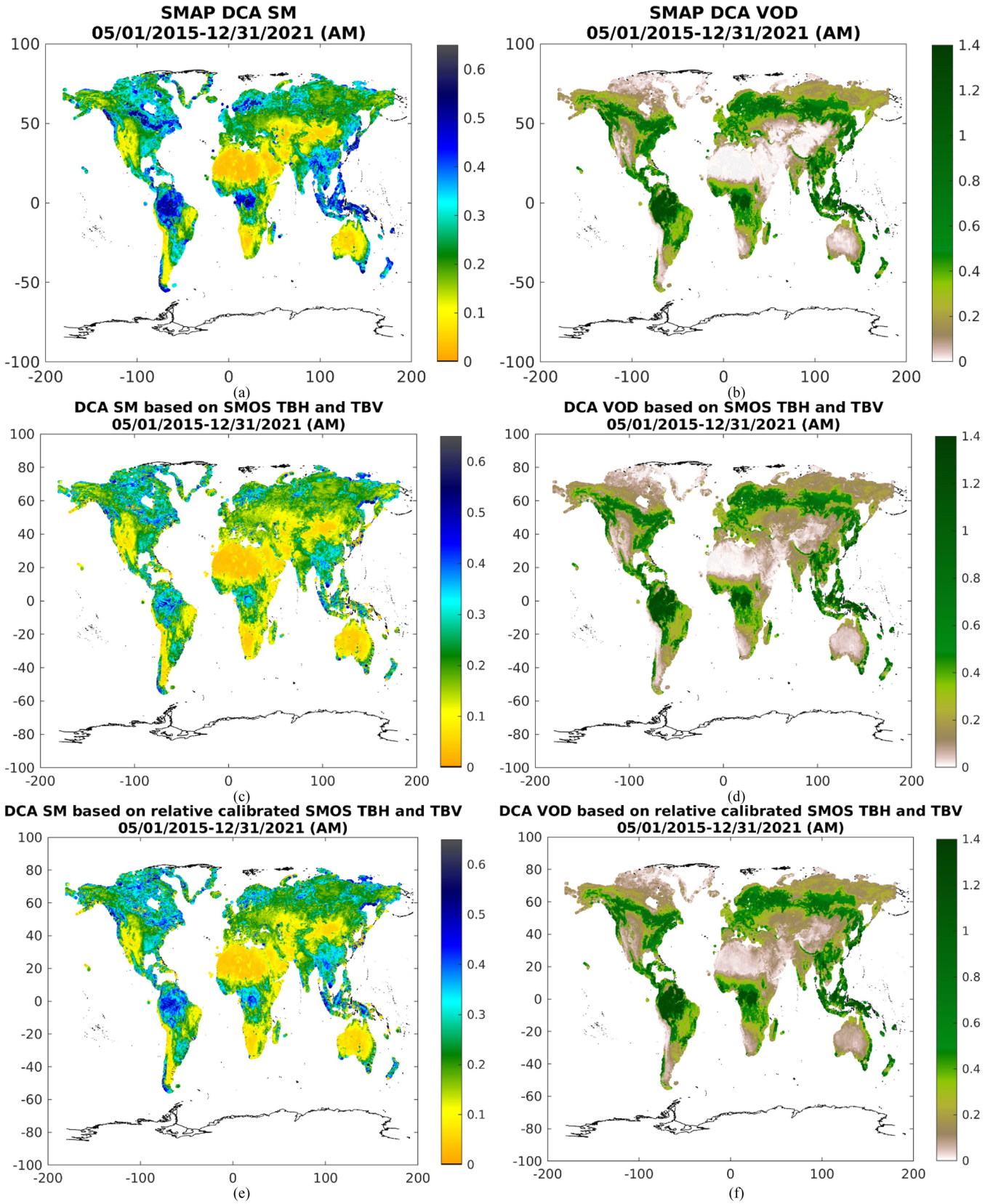

Fig. 10. Global Maps of averaged SM (right column) and VOD (left column) over the period between 1 May 2015 and 31 December 2021. (a) and (b): SMAP DCA SM and VOD. (c) and (d): DCA SM and VOD from SMOS based TBs before relative calibration. (e) and (f): DCA SM and VOD from SMOS based TBs after relative calibration.

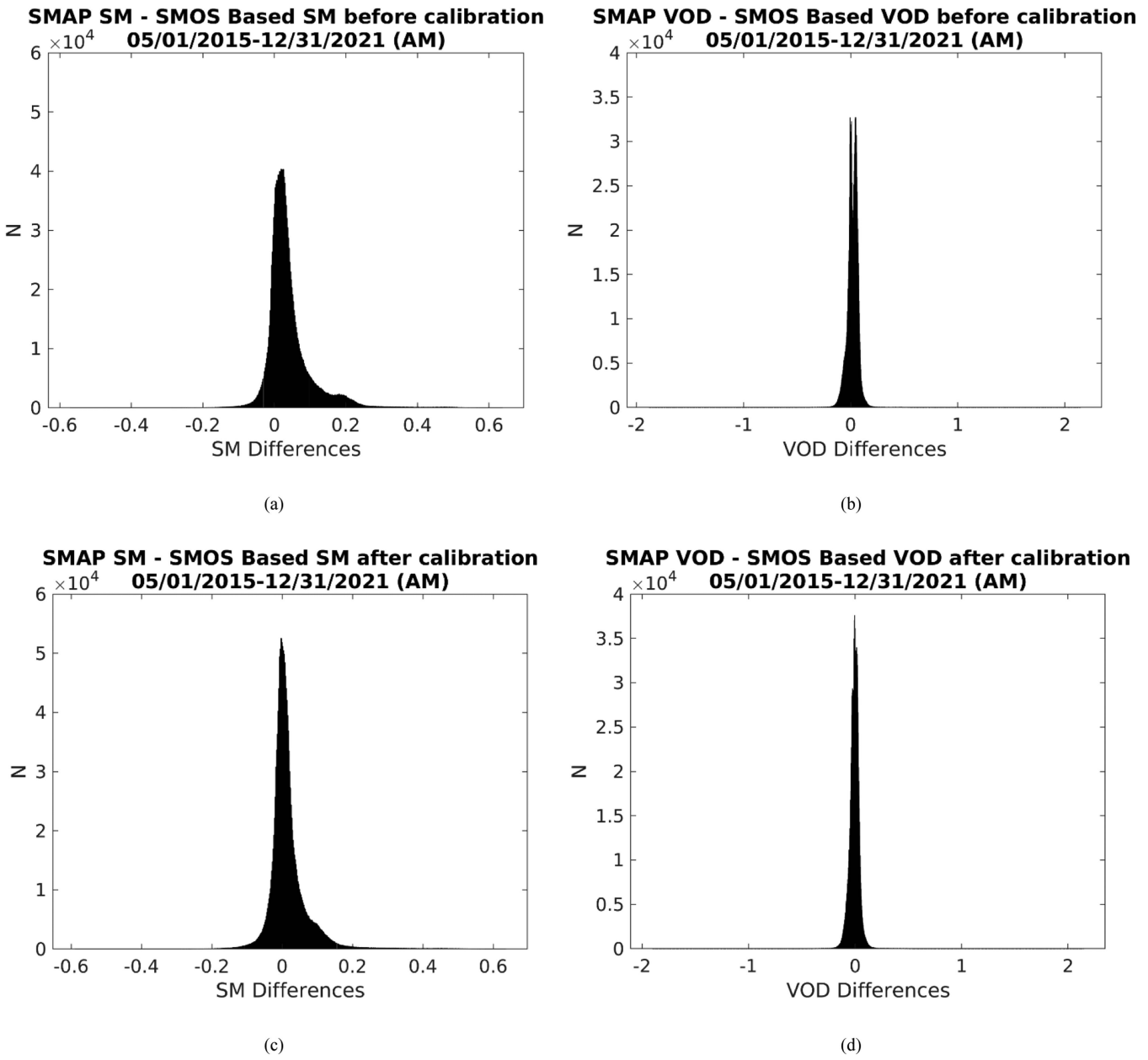

Fig. 11. Statistics of Global differences: (a) and (b) show differences before relative calibration for SM and VOD respectively and (c) and (d) show differences after relative calibration for SM and VOD respectively.

CVS [31] for SM and L-VOD based on SMAP, SMOS before relative calibration (BRC), and SMOS after the relative calibration (ARC). The figure shows a reduction of MD after relative calibration. In fact, the SMAP SM mean value was 0.19 m^3/m^3, while the SMOS-based SM mean values were 0.16 and 0.17 m^3/m^3 before and after the relative calibration, respectively. The SMAP VOD mean value was 0.19, while the SMOS-based VOD mean values were 0.14 and 0.18 before and after the relative calibration, respectively. Fig. 9 summarizes the mean values of SM and VOD over all the CVS, showing in all cases that the differences in mean values were reduced after the relative calibration was applied. Fig. 10(a) displays global maps of averaged SMAP SM for eight years of data from 1 May 2015 to 31 December 2021. Fig. 10(c) displays SM based on the SMOS TB before the relative calibration for the same period. It was observed that the SMOS SM showed a dry MD with respect to SMAP, especially in forested areas like the Amazon and Congo, the east coast of Asia, and at latitudes above 50°N. After the relative calibration [see Fig. 10(e)], the MD was reduced. Fig. 10(b), (d), and (f) displays global maps of the average VOD for the same period. Even though the observed patterns were very similar for the three images, there are clear differences, especially in the northeastern part of Africa, the Arabic peninsula, and the center of Asia, mostly caused by the presence of RFI. Fig. 11 shows the statistics of the SM and VOD differences between SMAP and SMOS based on the SM global maps before and after the relative calibration shown in Fig. 10. The mean value differences show improvement. Before the relative calibration, the MD was -0.041 m^3/m^3 and -0.019 for SM and VOD, respectively, while after the relative calibration,

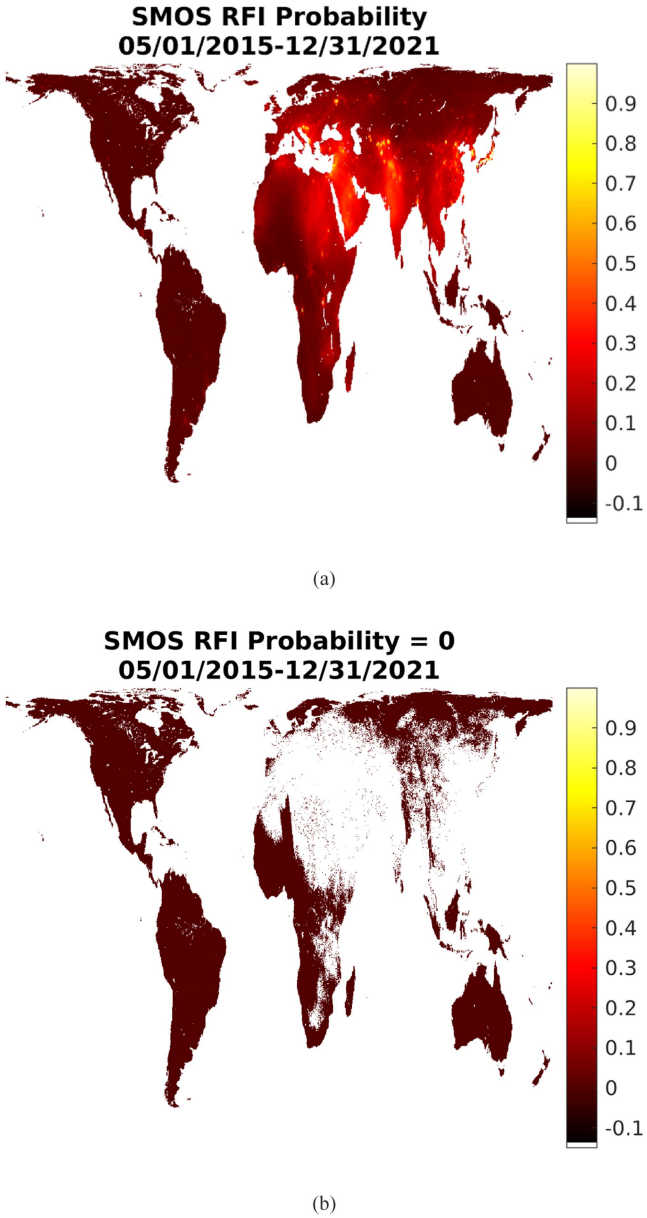

Fig. 12. (a) Global maps of averaged RFI probability obtained from the SMOS data product (1 May 2015–31 December 2021). (b) Global map of grid cells with RFI probability equal to zero.

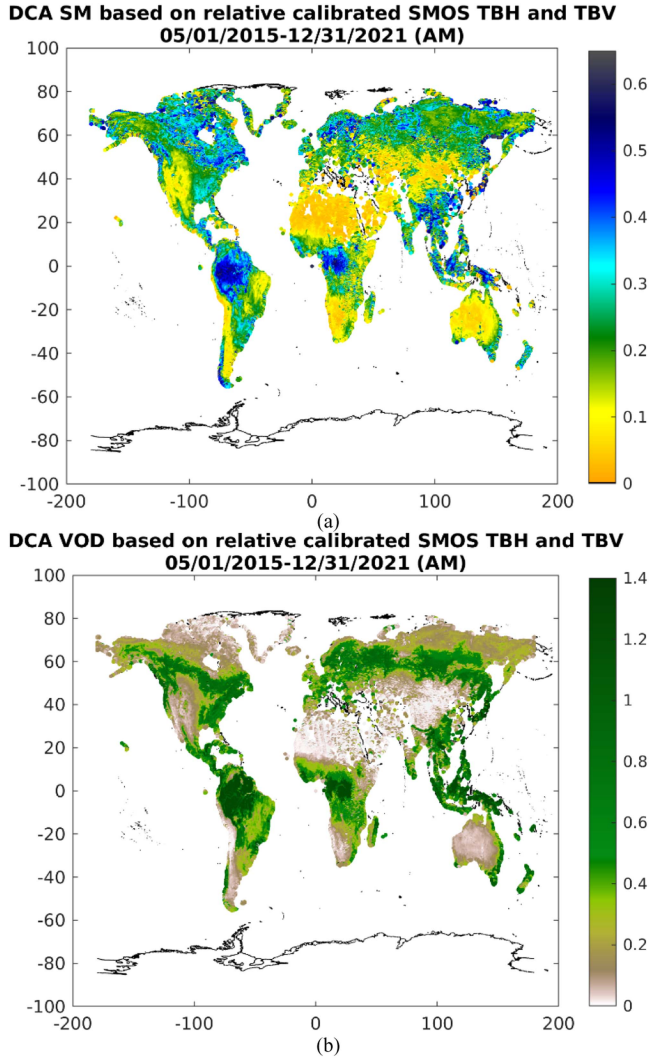

Fig. 13. (a) and (b) show global maps of SM and VOD after the data were filtered by RFI. Only data with a SMOS RFI probability equal to zero was considered.

the MD was reduced to -0.017 m^3/m^3 for SM and 0.0057 for VOD. The standard deviation also shows an improvement before and after the relative calibration, with values of 0.064 m^3/m^3 and 0.059 for SM and VOD before the relative calibration and 0.057 m^3/m^3 and 0.056 after the relative calibration.

C. Impact of RFI

Fig. 2 shows how the presence of RFI can affect the inter-calibration parameters and, therefore, the corresponding SM and VOD retrievals. Fig. 12 displays the global maps of RFI probability averaged over SMOS data from (1 May 2015–31 December 2021). It shows that most of the RFI affects substantial portions of Asia and North Africa. The map on the right shows the areas with zero RFI probability, where large areas of Asia and North Africa are missing. Fig. 13 shows global maps of SM and VOD after the data were filtered for RFI. Only data with an RFI probability equal to zero was considered. The areas with higher values of VOD over North Africa and Asia were removed due to the high RFI probability. Fig. 14 displays density plots of SM and VOD absolute differences (|SMOS-SMAP|) versus RFI probability. The red line displays the mean value by binned RFI probability value. The differences at each 2.5 probability bin were averaged and shown in red and is also displayed on the right column [see (b) and (d)] for clarity. For areas with probability values less than 0.4, the average SM differences stayed below 0.04 m^3/m^3; above 0.4, the SM differences increased when the RFI probability values increased. For the VOD, the difference increased linearly with the RFI probability value; above 0.4, the VOD differences were greater than 0.09. Fig. 15(a) displays the percentage of measurements for the period between 1 May 2015 and 31 December 2021 affected by RFI under different RFI probability thresholds. It shows that only 21% of the measurements were not affected by RFI but that 97% of measurements were affected by RFI

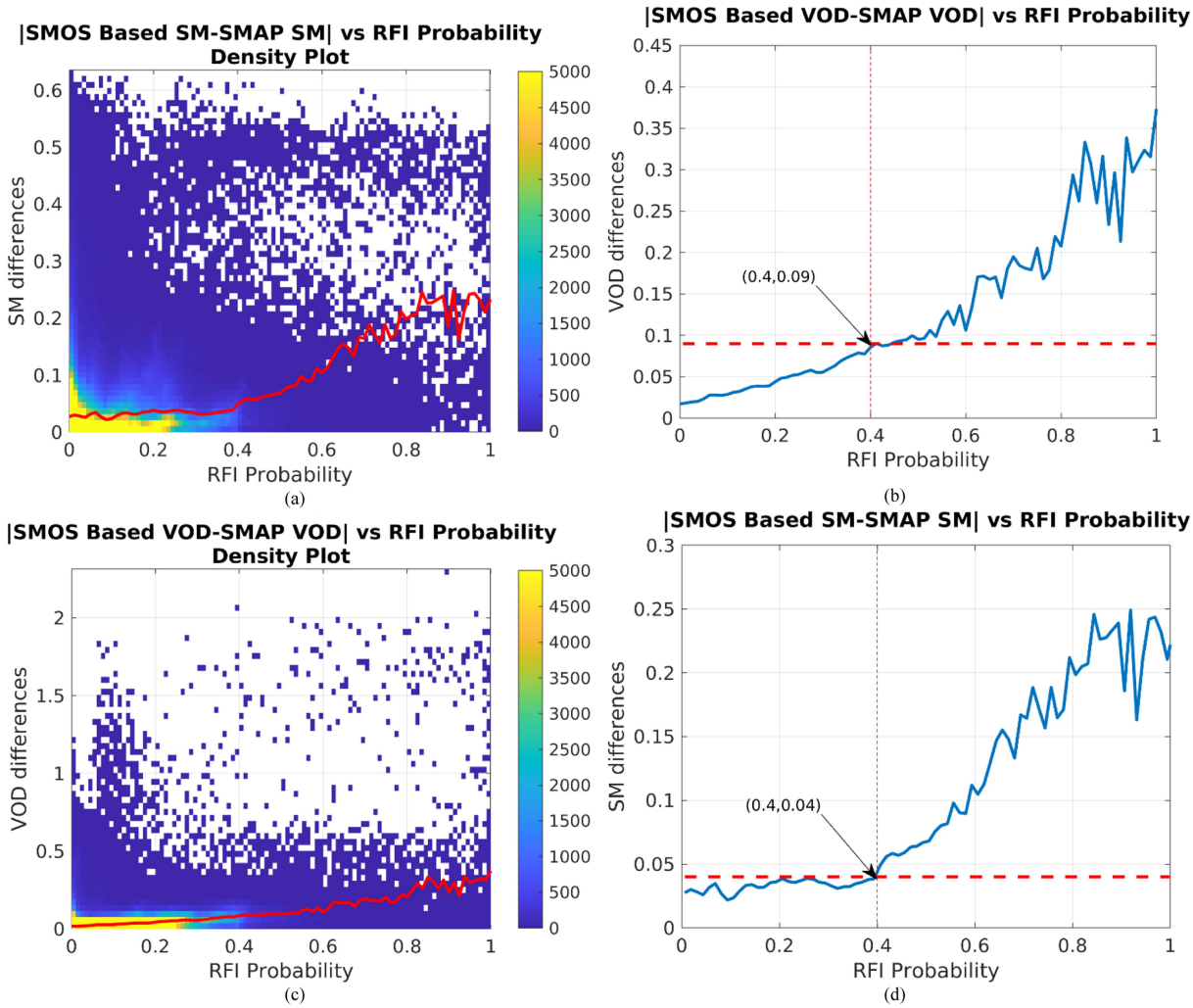

Fig. 14. (a) and (c) show density plots of SM and VOD differences (SMOS-SMAP) vs RFI probability. The red line displays the mean value by binned RFI probability value. The considered binned size was 2.5. On the right column (b) and (d), only the average values are displayed.

levels under 0.4. Fig. 15(b) displays the percentage of cells with RFI probability levels under different RFI thresholds. For each EASE-2 grid cell, the RFI probability level was averaged during the period 1 May 2015 and 31 December 2021. It shows that only 0.04% of cells were not affected by RFI at all and that 98.8% of the cells had an averaged level of RFI probability below 0.4.

D. Coverage Evaluation

Fig. 16 displays an example showing global coverage differences among the SMAP SM, SMOS SM, and SMOS-SMAP combined SM, using AM data on the date of 1 September 2017. For the combined data, average values were taken for overlapping pixels between SMAP and SMOS estimates. The example clearly shows the reduction in the daily gaps after the SMOS-SMAP integration. Fig. 17 shows the improvement in temporal coverage. We showed that the global mean number of visits to each grid went up from 283 (SMAP only) to 446 (SMAP+SMOS) when both AM and PM overpasses were considered, an improvement in coverage of 60% over SMAP only coverage. Considering only AM half-orbit passes, we saw that the average global number of visits was 223 times (1 visit every 1.6 days) for the combined product while it was 141 for SMAP only (1 visit every 2.5 days) and it was 82 times for the SMOS only product (1 visit every 4.4 days).

IV. Retrieval Assessment

A. SM Performance Evaluation

Table II presents the ubRMSD, MD, RMSD, and correlation (R) for the AM overpasses over the SMAP CVS (see [32], [33]). The approach, including the processing, quality checking, and filtering of the in situ SM, is the same as in the core site assessment described in [22]. The satellite data were filtered using the SMAP and SMOS quality flags (for the Twente and HOBE CVS, there were no good-quality data available). Table II shows that the ubRMSD is 0.036, 0.043, and 0.039 m^3/m^3 for the SMAP only, the SMOS only, and for the combined case, respectively. Table II indicates the averaged values when Twente and HOBE were included and when they were not. The averaged values when RFI is filtered are also shown. Table III presents the ubRMSD, MD, RMSD, and R for the PM overpasses, again with good-quality data not available over Twente and HOBE. Accordingly, ubRMSD is 0.035, 0.043, and 0.039 m^3/m^3 for

TABLE II
CVS ASSESSMENT. AM HALF-ORBIT PASSES WERE USED BETWEEN 1 MAY 2015 AND 31 DECEMBER 2021

Site Name	ubRMSD			MD			RMSD			R		
	SMAP	SMOS	COMBINED	SMAP	SMOS	COMBINED	SMAP	SMOS	COMBINED	SMAP	SMOS	COMBINED
Reynolds Creek	0.044	0.043	0.044	−0.014	−0.011	−0.013	0.046	0.044	0.046	0.630	0.640	0.620
Walnut Gulch	0.029	0.037	0.032	0.029	0.035	0.031	0.041	0.051	0.045	0.680	0.670	0.680
TxSON	0.025	0.028	0.027	0.003	−0.011	−0.002	0.025	0.030	0.027	0.930	0.900	0.910
Fort Cobb	0.032	0.032	0.032	−0.045	−0.047	−0.046	0.056	0.057	0.056	0.880	0.870	0.880
Little Washita	0.027	0.030	0.028	−0.007	−0.006	−0.006	0.028	0.030	0.029	0.910	0.900	0.900
South Fork	0.040	0.048	0.043	−0.046	−0.041	−0.044	0.061	0.063	0.061	0.770	0.680	0.730
Little River	0.040	0.039	0.040	0.040	0.045	0.042	0.057	0.059	0.058	0.780	0.780	0.770
Kenaston	0.031	0.036	0.033	0.005	0.008	0.006	0.031	0.037	0.033	0.790	0.730	0.770
Carman	0.053	0.052	0.053	−0.065	−0.076	−0.069	0.084	0.092	0.087	0.660	0.650	0.660
Monte Buey	0.033	0.063	0.046	−0.023	−0.035	−0.027	0.040	0.072	0.053	0.850	0.560	0.740
REMEDHUS	0.035	0.041	0.038	0.007	−0.008	0.003	0.036	0.041	0.038	0.840	0.760	0.810
Twente	0.054	0.092	0.071	−0.020	−0.059	−0.033	0.058	0.109	0.078	0.850	0.540	0.730
HOBE	0.035	0.038	0.036	−0.011	−0.003	−0.008	0.036	0.038	0.037	0.790	0.830	0.820
Mongolia	0.030	0.026	0.029	−0.019	−0.011	−0.017	0.035	0.028	0.033	0.800	0.880	0.820
Yanco	0.034	0.035	0.034	0.018	0.019	0.019	0.039	0.040	0.039	0.920	0.920	0.920
AVERAGE	0.036	0.043	0.039	−0.010	−0.013	−0.011	0.045	0.053	0.048	0.805	0.754	0.784
AVERAGE Without Twente and Hobe	0.035	0.039	0.037	−0.009	−0.011	−0.009	0.045	0.050	0.047	0.765	0.785	0.762
Average filtering RFI	0.035	0.035	0.035	−0.009	−0.010	−0.009	0.045	0.048	0.045	0.803	0.787	0.801

TABLE III
CVS ASSESSMENT

Site Name	ubRMSD			MD			RMSD			R		
	SMAP	SMOS	COMBINED	SMAP	SMOS	COMBINED	SMAP	SMOS	COMBINED	SMAP	SMOS	COMBINED
Reynolds Creek	0.048	0.046	0.047	−0.015	−0.015	−0.015	0.050	0.048	0.049	0.550	0.710	0.620
Walnut Gulch	0.026	0.028	0.027	0.014	0.016	0.014	0.029	0.032	0.030	0.650	0.670	0.650
TxSON	0.022	0.029	0.025	0.000	0.002	0.000	0.022	0.029	0.025	0.930	0.880	0.910
Fort Cobb	0.030	0.031	0.030	−0.054	−0.050	−0.053	0.062	0.059	0.061	0.870	0.870	0.870
Little Washita	0.026	0.029	0.027	−0.007	−0.007	−0.007	0.027	0.030	0.028	0.900	0.880	0.890
South Fork	0.038	0.037	0.037	−0.054	−0.049	−0.052	0.066	0.061	0.064	0.780	0.780	0.790
Little River	0.038	0.038	0.038	0.044	0.043	0.044	0.058	0.058	0.058	0.760	0.730	0.750
Kenaston	0.030	0.032	0.031	0.005	0.013	0.008	0.031	0.034	0.032	0.840	0.800	0.820
Carman	0.049	0.049	0.049	−0.073	−0.078	−0.075	0.088	0.092	0.089	0.580	0.640	0.600
Monte Buey	0.033	0.045	0.039	−0.026	−0.032	−0.027	0.042	0.055	0.047	0.800	0.660	0.730
REMEDHUS	0.034	0.039	0.036	−0.007	−0.007	−0.007	0.035	0.040	0.037	0.850	0.820	0.840
Twente	0.053	0.083	0.068	−0.021	−0.072	−0.037	0.056	0.110	0.078	0.850	0.600	0.750
HOBE	0.039	0.089	0.060	−0.005	−0.009	−0.006	0.040	0.090	0.060	0.760	0.630	0.680
Mongolia	0.030	0.041	0.033	−0.017	−0.009	−0.015	0.035	0.042	0.036	0.700	0.690	0.680
Yanco	0.033	0.030	0.032	0.011	0.010	0.011	0.035	0.031	0.034	0.920	0.930	0.920
AVERAGE	0.035	0.043	0.039	−0.014	−0.016	−0.014	0.045	0.054	0.049	0.783	0.753	0.767
AVERAGE Without Twente and Hobe	0.034	0.036	0.035	−0.014	−0.013	−0.013	0.045	0.047	0.045	0.779	0.774	0.775
Average filtering RFI	0.034	0.033	0.034	−0.014	−0.010	−0.014	0.045	0.046	0.045	0.779	0.751	0.777

PM half-orbit passes were used between 1 May 2015 and 31 December 2021.

SMAP only, the SMOS only, and for the combined case, respectively. Similarly to Tables II, Table III indicates the average values when Twente and HOBE were included and when they were not. Note that there while the SMAP official SM product has accuracy requirements there are no such requirements for the SMOS-based SM. Still, the combined product meets the requirement of both missions with an accuracy of less than 0.040 m^3/m^3 (see [1], [4]).

B. Vegetation Optical Depth Evaluation

The correlation between the SMAP VOD and two vegetation parameters, tree height (H) [34] and the above ground biomass (B) [35] commonly associated with VOD, was analyzed. Both datasets were aggregated to the 9-km EASE-2 to match the SMAP and SMOS-based data grid, as shown in Fig. 18. Fig. 19 displays a global-scale density plot of the spatial relationship between SMOS-based VOD and SMAP VOD and biomass (B) and tree height (H). The black line represents the linear regression fitting of mean value bins. The VOD axis was divided into a 0.05 bin size with the tree height or biomass means averaged within those bins. Then, the linear fitting through those average values was computed. The relationship between those parameters and the VOD is clearly linear.

The biomass (B) is related to a the SMAP VOD and SMOS VOD by

$$B_{\text{smap}} = 190.78\ \text{VOD} - 45.15 \tag{5}$$

$$B_{\text{smos}} = 209.62\ \text{VOD} - 51.49. \tag{6}$$

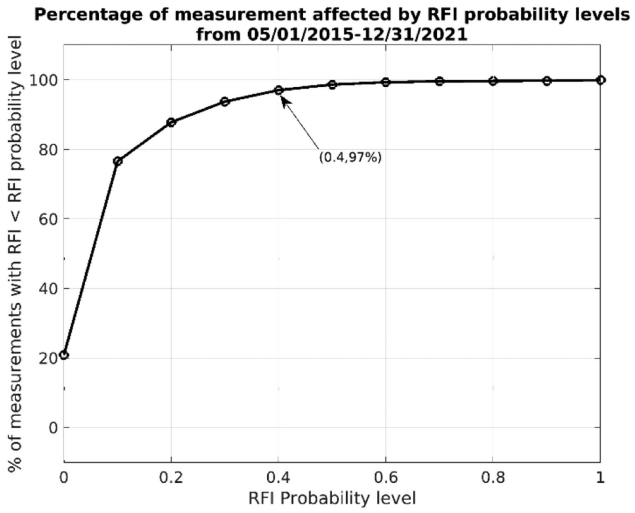

(a)

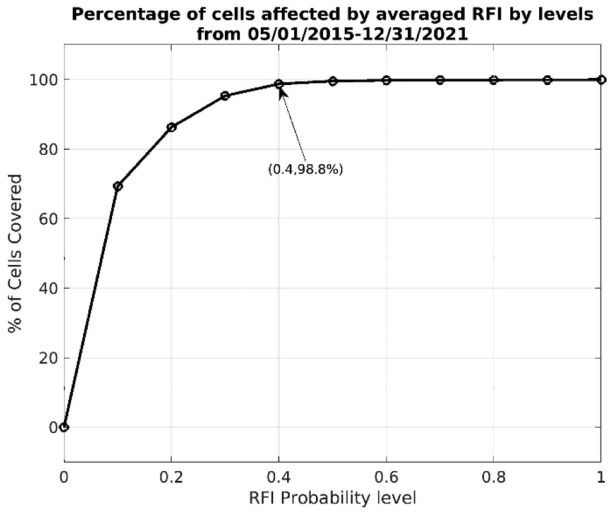

(b)

Fig. 15. Data obtained between 1 May 2015 and 31 December 2021. (a) Percentage of successful SM retrievals by RFI probability levels. (b) Percentage of cells with RFI under different probability levels after averaging RFI probability for each cell during the indicated period.

Equations (5) and (6) led to a modeled difference smaller than 12.5 Mg/ha for a VOD smaller than 1, showing the consistency between SMAP VOD and the SMOS-based VOD. The spatial correlation (R) between SMAP VOD and SMOS-based VOD with respect to B is $R = 0.76$ and $R = 0.79$, respectively.

The tree height (H) was related to a the SMAP VOD and SMOS VOD by

$$H_{\text{smap}} = 16.98\ \text{VOD} + 8.317 \tag{7}$$

$$H_{\text{smos}} = 15.85\ \text{VOD} + 8.443 \tag{8}$$

leading to a modeled difference smaller than 1 meter for a VOD smaller than 1. The spatial correlation (R) between SMAP VOD

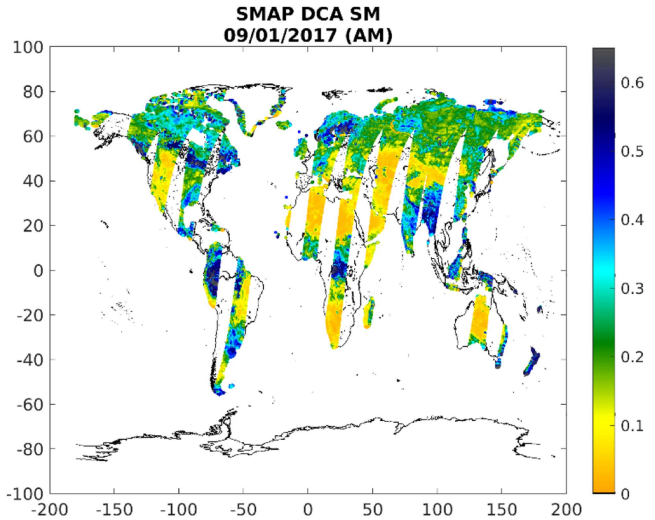

(a)

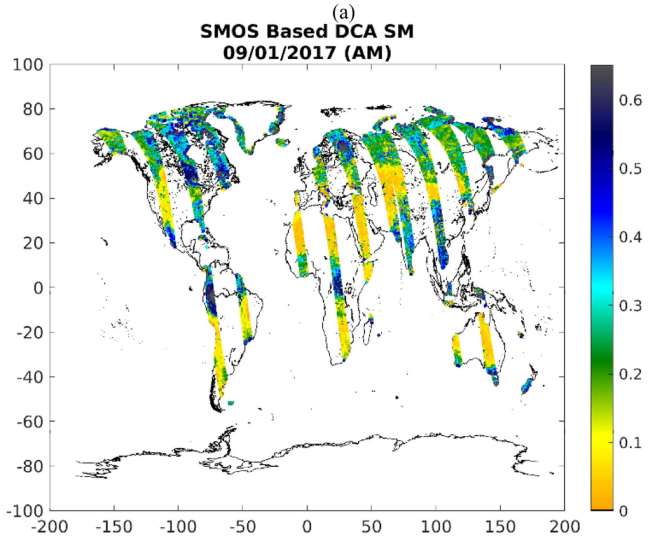

(b)

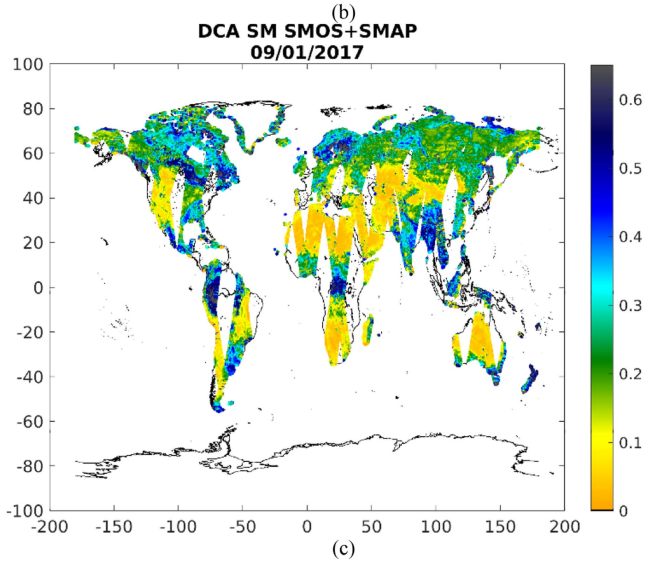

(c)

Fig. 16. (a), (b), and (c) show global coverage for AM data on September 1, 2017. (a) SMAP SM. (b) SMOS SM. (c) SMOS-SMAP combined SM. For the combined data, average values were taken for overlapping pixels between SMAP and SMOS estimates.

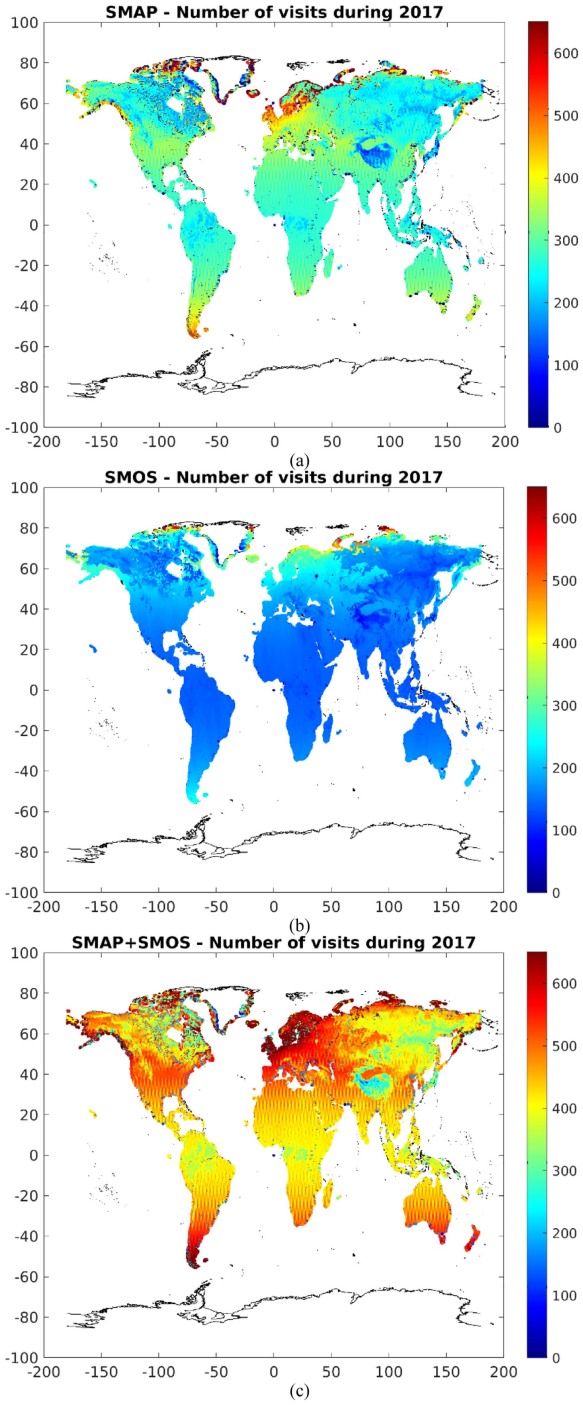

Fig. 17. (a) Show the number of visits throughout 2017 for SMAP only. (b) SMOS only. (c) The combine SMOS-SMAP products.

and SMOS-based VOD with respect to H is $R = 0.82$ and $R = 0.83$, respectively. Again, this is an indication of the consistency between SMAP and the SMOS-based TB data. The observed bias in the density plots, H and B should be zero for VOD equal zero, it could be caused by the effect of surface roughness, which it is well known to affect the retrieval of VOD.

V. Discussion and Summary

A combined SMAP-SMOS data product was developed (see [36], [37]) utilizing an RC of the SMOS TB observations

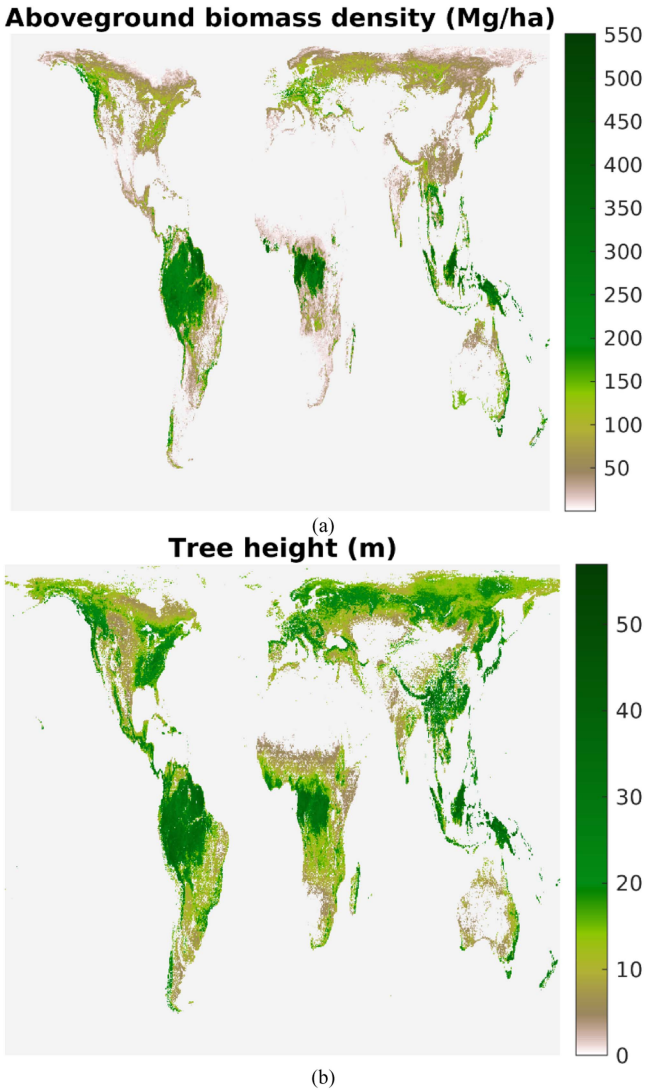

Fig. 18. (a) Aboveground biomass density of vegetation in units of Mg/ha. (b) Tree height (meters).

interpolated to 40° incidence angle. Following the algorithm detailed in [27], the SMOS measurements at the antenna were transformed into TBs at the Earth's level, generating TBs for H and V polarizations for all the SMOS incidence angles. Using the TB as a function of incidence angles, the TB at 40° was obtained by linear interpolation. The RC parameters were obtained by a comparison of the SMAP and SMOS footprint TB measurements following the criteria match up described in Section II-B. The RC parameters were then applied to each orbit pass to the SMOS TB collocated to the SMAP 9 km EASE 2 grid to generate SMAP-like (RC) SMOS TBs. Unlike the authors in [25] and [26] produced a set of SMOS-like SMAP data to generate a combined SMOS-SMAP product to retrieve SM and VOD or see ice thickness, this work is the first official product to relatively calibrate the SMOS TBs to SMAP, generating a SMAP-like SMOS TB that allows us to develop SMOS-based SM and VOD products consistent with the SMAP products.

The evaluation of differences between SMOS-based TBs, before and after relative calibration, and the SMAP TBs shows

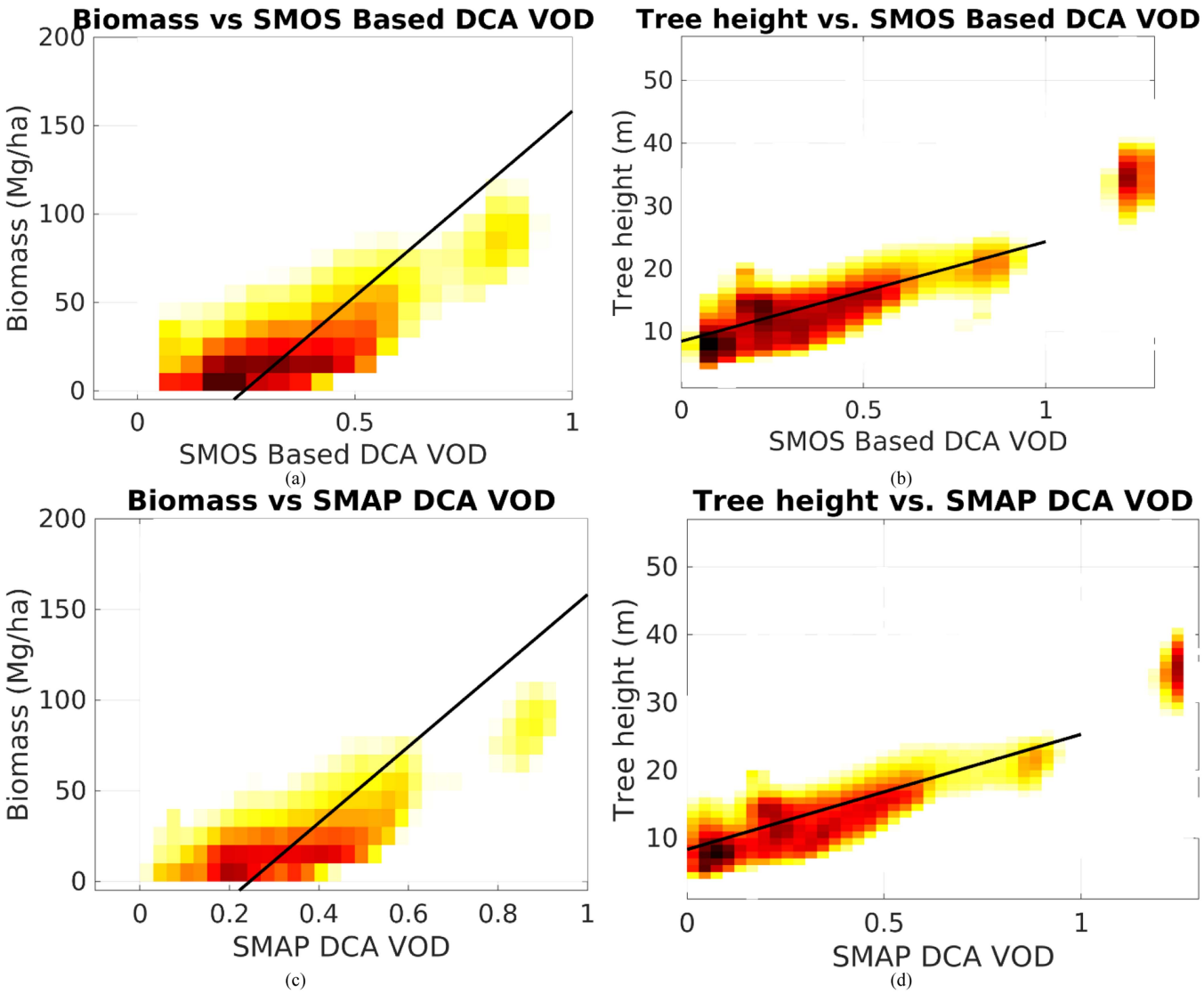

Fig. 19. Global-scale density plot of the spatial relationship between SMOS Based VOD and the Biomass (a) and Tree Height (b) and SMAP VOD and the Biomass (c) and Tree Height (d). The black line represents the linear regression fitting.

that we successfully generated a consistent SMAP-like SMOS TBs at 40° incidence angles. Indeed, we showed that the MDs between the RC SMOS TBs and the SMAP TBs were reduced from 0.5 to −0.03 K for TB H and from 2.6 to 0.014 K for TB V for the AM half-orbit passes. For the PM half-orbit passes the mean values of differences were reduced from 0.82 to 0.27 K and from 2.88 to 0.19 K for TB H and TB V, respectively. Using RC SMOS TBs at 40° together with the SMAP ancillary data and the SMAP retrieval algorithm (DCA), we were able to retrieve SM and VOD consistent with the SMAP enhanced SM and VOD products. It was shown that, over the CVSs, the combined SM time series satisfied the SMAP requirement with 0.039 m3/m3 ubRMSD for AM and PM half-orbit passes. It was also shown that the retrieved VOD from SMAP TBs and the RC SMOS TBs were consistent with biomass and tree-height data leading to the linear relations in (5), (6), (7), and (8). The spatial correlation (R) between SMAP VOD and SMOS-based VOD, with respect to B, is $R = 0.76$ and $R = 0.79$, respectively, showing a slight difference in favor of the SMOS data. The correlation (R) between SMAP VOD and SMOS-based VOD, with respect to H, is $R = 0.82$ and $R = 0.83$, respectively. It is well known that there is no reference for the performance of VOD and so the use of those parameters, as common as it is, needs to be better understood. The observed offset indicates that the retrieval of VOD is being affected by other factors. We know from the tau-omega model utilized to model TB that the surface roughness plays an important role, and it is hard to separate its influence from the VOD effects. We, thus, suspect that the observed offset is caused, in part, by the roughness of surface. Recent work proposed the development of a high spatial resolution canopy water content (CWC) product [38]. This product, derived from Sentinel-2, Landsat-8, and MODIS would provide another biophysical parameter that would not only help in the evaluation of retrieved L-band VOD but would also potentially provide insight for the contribution of CWC to the VOD retrievals.

This study also indicates that filtering the data using the RFI probability is recommended in order to remove the impact on SM

and VOD retrievals. It was shown that using an RFI probability level of 0.4% as a threshold could lead to better quality retrievals with minimal loss of data.

With respect to the coverage, we showed that by producing a combined SMAP-SMOS product, we were able to increase the global average revisit time by 60% when the AM and PM were considered together and when only AM passes were considered, the revisit frequency was reduced by one day average globally.

Although the effort resulted in an official product, there is more work to be done in the future. The extension of this work to ocean data could lead to a combined SMAP-SMOS salinity product. The SMAP team would also like to extend the dataset of SMAP-like SMOS TB, currently from 2015 to 2021, to 2010 to the present.

REFERENCES

[1] D. Entekhabi et al., "The soil moisture active passive (SMAP) mission," *Proc. IEEE*, vol. 98, no. 5, pp. 704–716, May 2010.

[2] S.K. Chan et al., "Assessment of the SMAP passive soil moisture product," *IEEE Trans. Geosci. Remote Sens.*, vol. 54, no. 8, pp. 4994–5007, Aug. 2016.

[3] Y.H. Kerr, P. Waldteufel, J.-P. Wigneron, J. Martinuzzi, J. Font, and M. Berger, "Soil moisture retrieval from space: The soil moisture and ocean salinity (SMOS) mission," *IEEE Trans. Geosci. Remote Sens.*, vol. 39, pp. 1729–1735, Aug. 2001.

[4] Y.H. Kerr et al., "The SMOS mission: New tool for monitoring key elements of global water cycle," *Proc. IEEE*, vol. 98, no. 5, pp. 666–687, May 2010.

[5] D. Entekhabi, S. Yueh, P. O'Neill, and K. Kellogg, in *SMAP Handbook—Soil Moisture Active Passive: Mapping Soil Moisture and Freeze/Thaw From Space*, SMAP Project, Jet Propulsion Laboratory, Pasadena, CA, USA, 2014.

[6] J. R. Piepmeier et al., "GSMAP L-band microwave radiometer: Instrument design and first year on orbit," *IEEE Trans. Geosci. Remote Sens.*, vol. 55, no. 4, pp. 1954–1966, Apr. 2017, doi: 10.1109/tgrs.2016.2631978.

[7] K. D. McMullan et al., "SMOS: The payload," *IEEE Trans. Geosci. Remote Sens.*, vol. 46, no. 3, pp. 594–605, Mar. 2008, doi: 10.1109/TGRS.2007.914809.

[8] M. Martín-Neira et al., "SMOS instrument performance and calibration after six years in orbit," *Remote Sens. Environ.*, vol. 180, pp. 19–39, 2016, doi: 10.1016/j.rse.2016.02.036.

[9] S. Mecklenburg et al., "ESA's soil moisture and ocean salinity mission: Mission performance and operations," *IEEE Trans. Geosci. Remote Sens.*, vol. 50, no. 5, pp. 1354–1366, May 2012, doi: 10.1109/TGRS.2012.2187666.

[10] S. Fournier et al., "Quantification of Aquarius, SMAP, SMOS and argo-based gridded sea surface salinity product sampling errors," *Remote Sens.*, vol. 15, 2023, Art. no. 422, doi: 10.3390/rs15020422.

[11] R. Fernandez-Moran et al., "SMOS-IC: An alternative SMOS soil moisture and vegetation optical depth product," *Remote Sens.*, vol. 9, no. 5, 2017, Art. no. 457, doi: 10.3390/rs9050457.

[12] A. Colliander et al., "Performance of SMOS soil moisture products over core validation sites," *IEEE Geosci. Remote Sens. Lett.*, vol. 20, 2023, Art. no. 2502805, doi: 10.1109/lgrs.2023.3272878.

[13] K. A. McColl, S. H. Alemohammad, R. Akbar, A. G. Konings, S. Yueh, and D. Entekhabi, "The global distribution and dynamics of surface soil Moisture," *Nature Geosci.*, vol. 10, no. 2, pp. 100–104, 2017, doi: 10.1038/ngeo2868.

[14] K. A. McColl et al., "Global characterization of surface soil moisture Drydowns," *Geophys. Res. Lett.*, vol. 44, no. 8, pp. 3682–3690, 2017.

[15] K. A. McColl, Q. He, H. Lu, and D. Entekhabi, "Short-term and long-term surface soil moisture memory time scales are spatially anticorrelated at global scales," *J. Hydrometeor.*, vol. 20, pp. 1165–1182, 2019, doi: 10.1175/JHM-D-18-0141.1.

[16] R. Oliva et al., "SMOS radio frequency interference scenario: Status and actions taken to improve the RFI environment in the 1400–1427-MHz passive band," *IEEE Trans. Geosci. Remote Sens.*, vol. 50, no. 5, pp. 1427–1439, May 2012, doi: 10.1109/tgrs.2012.2182775.

[17] R. J. Piepmeier et al., "Radio- frequency interference mitigation for the soil moisture active passive microwave radiometer," *IEEE Trans. Geosci. Remote Sens.*, vol. 52, no. 1, pp. 761–775, Jan. 2014, doi: 10.1109/tgrs.2013.2281266.

[18] P. N. Mohammed, M. Aksoy, J. R. Piepmeier, J. T. Johnson, and A. Bringer, "SMAP L-band microwave radiometer: RFI mitigation prelaunch analysis and first year on-orbit observations," *IEEE Trans. Geosci. Remote Sens.*, vol. 54, no. 10, pp. 6035–6047, Oct. 2016, doi: 10.1109/tgrs.2016.2580459.

[19] M. S. Burgin et al., "Comparative study of the SMAP passive soil moisture product with existing satellite-based soil moisture products," *IEEE Trans. Geosci. Remote Sens.*, vol. 55, no. 5, pp. 2959–2971, May 2017, doi: 10.1109/tgrs.2017.2656859.

[20] H. Cui et al., "Evaluation and analysis of AMSR-2, SMOS, and SMAP soil moisture products in the Genhe area of China," *J. Geophys. Res.: Atmospheres*, vol. 122, no. 16, pp. 8650–8666, 2017, doi: 10.1002/2017jd026800.

[21] B. G. Mousa and H. Shu, "Spatial evaluation and assimilation of SMAP, 'SMOS, and ASCAT satellite soil moisture products over Africa using statistical techniques," *Earth Space Sci.*, vol. 7, no. 1, 2020, Art. no. e2019EA000841, doi: 10.1029/2019ea000841.

[22] Z. Wang, T. Che, T. Zhao, L. Dai, X. Li, and J.-P. Wigneron, "Evaluation of SMAP, SMOS, and AMSR2 soil moisture products based on distributed ground observation network in cold and arid regions of China," *IEEE J. Sel. Topics Appl. Earth Observ. Remote Sens.*, vol. 14, pp. 8955–8970, 2021, doi: 10.1109/jstars.2021.3108432.

[23] A. Colliander et al., "Performance of SMOS Soil moisture products over core validation sites," *IEEE Geosci. Remote Sens. Lett.*, vol. 20, 2023, Art. no. 2502805, doi: 10.1109/lgrs.2023.3272878.

[24] R. Bindlish, S. Chan, A. Colliander, Y. Kerr, and T. J. Jackson, "Integrated SMAP and SMOS soil moisture observations," in *Proc. IGARSS IEEE Int. Geosci. Remote Sens. Symp.*, 2019, pp. 5370–5373, doi: 10.1109/IGARSS.2019.8900109.

[25] X. Li et al., "The first global soil moisture and vegetation optical depth product retrieved from fused SMOS and SMAP L-band observations," *Remote Sens. Environ.*, vol. 282, 2022, Art. no. 113272, doi: 10.1016/j.rse.2022.113272.

[26] C. Paţilea, G. Heygster, M. Huntemann, and G. Spreen, "Combined SMAP–SMOS thin sea ice thickness retrieval," *Cryosphere*, vol. 13, pp. 675–691, 2019, doi: 10.5194/tc-13-675-2019.

[27] T. Zhao et al., "Refinement of SMOS multiangular brightness temperature toward soil moisture retrieval and its analysis over reference targets," *IEEE J. Sel. Topics Appl. Earth Observ. Remote Sens.*, vol. 8, no. 2, pp. 589–603, Feb. 2015, doi: 10.1109/JSTARS.2014.2336664.

[28] J. Chaubell et al., "Improving brightness temperature measurements near coastal areas for SMAP," *IEEE J. Sel. Topics Appl. Earth Observ. Remote Sens.*, vol. 12, no. 11, pp. 4578–4588, Nov. 2019, doi: 10.1109/JSTARS.2019.2951323.

[29] J. Chaubell et al., "Regularized dual-channel algorithm for the retrieval of soil moisture and vegetation optical depth from SMAP measurements," *IEEE J. Sel. Topics Appl. Earth Observ. Remote Sens.*, vol. 15, pp. 102–114, 2022, doi: 10.1109/JSTARS.2021.3123932.

[30] S. K. Chan et al., "Development and assessment of the SMAP enhanced passive soil moisture product," *Remote Sens. Environ.*, vol. 204, pp. 931–941, 2018.

[31] T. G. Caldwell et al., "The Texas soil observation network: A comprehensive soil moisture dataset for Remote sensing and land surface model validation," *Vadose Zone J.*, vol. 18, 2019, Art. no. 100034, doi: 10.2136/vzj2019.04.0034.

[32] P. O'Neill et al., in *Calibration and Validation for the L2/3_SM_P Version 6 and L2/3_SM_P_E Version 3 Data Products*, Jet Propulsion Laboratory, Pasadena, CA, USA, SMAP Project, JPL D-56297,, Aug. 2019.

[33] A. Colliander et al., "Validation of SMAP surface soil moisture products with core validation sites," *Remote Sens. Environ.*, vol. 191, pp. 215–231, 2017, doi: 10.1016/j.rse.2017.01.021.

[34] M. Simard, N. Pinto, J. Fisher, and A. Baccini, "Mapping forest canopy height globally with spaceborne LiDAR," *J. Geophys. Res.*, vol. 116, 2011, Art. no. G04021, doi: 10.1029/2011JG001708.

[35] V. Avitabile et al., "An integrated pan-tropical biomass map using multiple reference datasets," *Glob. Change Biol.*, vol. 22, no. 4, pp. 1406–1420, Oct. 2016, doi: 10.1111/gcb.13139.

[36] J. Chaubell et al., "SMOS-based SMAP L2 radiometer half- orbit 9 km EASE-grid soil moisture," National Snow and Ice Data Center, Boulder, CO USA, Rep. no. NSIDC-0799, 2025, doi: 10.5067/GXBB46ZD0CLE.

[37] J. Chaubell et al., "SMAP/SMOS L3 radiometer 9 km EASE- grid soil moisture,"National Snow and Ice Data Center, Boulder, CO, USA, Rep. no. NSIDC-0800, 2025, doi: 10.5067/E1NLXI1VJJ7M.
[38] H. Ma et al., "Satellite canopy water content from Sentinel-2, Landsat-8 and MODIS: Principle, algorithm and assessment," *Remote Sens. Environ.*, vol. 326, 2025, Art. no. 114801, doi: 10.1016/j.rse.2025.114801.

Julian Chaubell received the Bachelor of Science degree in mathematic from the University of Mar del Plata, Buenos Aires, Argentina, in 1997 and the Ph.D. degree in applied and computational mathematics from the California Institute of Technology, Pasadena, CA, USA, in 2004.

His doctoral work focused on low-coherence interferometric imaging. In April 2004, he joined Jet Propulsion Laboratory (JPL), Pasadena, CA, USA, as a Postdoctoral Research Associate in the Tracking Systems and Applications Section, where he worked on the modeling of EM-wave propagation in fully three-dimensional atmospheric refractive index distributions. In April 2007, he joined the Radar Science and Engineering section, JPL as a permanent employee where he has been working on the forward modeling of radar and radiometer measurements as well as retrieval of the geophysical quantity from those measurements. He has also been involved in electromagnetic modeling of electrically large aperture systems and structures. He was a part of the SMAP Instrument Operations Team and SMAP Radar L1 Subsystem Team. He is currently a part of the SMAP Radiometer L1 Team and SMAP Soil Moisture L2 Team.

Simon H. Yueh (Fellow, IEEE) received the Ph.D. degree in electrical engineering from the Massachusetts Institute of Technology, Cambridge, MA, USA, in January 1991.

He was a Postdoctoral Research Associate with the Massachusetts Institute of Technology from February to August 1991. In September 1991, he joined the Radar Science and Engineering Section, Jet Propulsion Laboratory (JPL), Pasadena, CA, USA, and has assumed various engineering and science management responsibilities. He was the Project Scientist of the National Aeronautics and Space Administration (NASA) Aquarius mission from January 2012 to September 2013, the Deputy Project Scientist of NASA Soil Moisture Active Passive Mission from January 2013 to September 2013, and the SMAP Project Scientist since October 2013. He has been the Principal/Co-Investigator of numerous NASA and DOD research projects on remote sensing of ocean salinity, ocean wind, terrestrial snow, and soil moisture. He has authored four book chapters and published more than 200 publications and presentations.

Dr. Yueh was the recipient the 2014 IEEE GRSS Transaction Prize Paper award, 2010 IEEE GRSS Transaction Prize Paper award, 2002 IEEE GRSS Transaction Prize Paper award, the 2000 Best Paper Award in the IEEE International Geoscience and Remote Symposium 2000, and the 1995 IEEE GRSS Transaction Prize Paper award for a paper on polarimetric radiometry. He was also the JPL Lew Allen Award in 1998, JPL Ed Stone Award in 2003, NASA Exceptional Technology Achievement Award in 2014 and NASA Outstanding Public Leadership Medal in 2017. He was an Associate Editor of Radio Science from 2003 to 2007. He is a member of the American Geophysical Union, Editor in Chief of IEEE TRANSACTIONS OF GEOSCIENCE AND REMOTE SENSING, a member of URSI Commission F.

Andreas Colliander received the M.Sc. (Tech.), Lic.Sc. (Tech.), and D.Sc. (Tech.) degrees in electrical and communications engineerin from Aalto University, Espoo, Finland, in 2002, 2005, and 2007, respectively.

He is currently a Senior Scientist with the Finnish Meteorological Institute, Helsinki, Finland. From 2008 to 2025, he was with the Jet Propulsion Laboratory, California Institute of Technology, Pasadena, CA USA, where he focused on developing microwave remote sensing techniques and led the calibration and validation of the geophysical retrievals of NASA's SMAP mission.

Akiko Hayashi received the B.S. degree in civil engineering and the M.S. degree in structural engineering from Duke University, Durham, NC, USA, in 1982 and 1984, respectively.

She is currently an Applications Software Engineer with the Ocean Circulation and Air Sea Interaction Group, Jet Propulsion Laboratory, Pasadena, CA USA, doing multimission (altimetry, SMAP, SMOS and NISAR) support for data processing, Level-3 and 4 product generation, matchup of auxiliary data for SSS retrievals, soil moisture retrievals, and their associated calibration and validation activities.

Rajat Bindlish (Senior Member, IEEE) received the B.S. degree in civil engineering from the Indian Institute of Technology, Bombay, Mumbai, India, in 1993 and the M.S. and Ph.D. degrees in civil engineering from The Pennsylvania State University, University Park, PA, USA, in 1996 and 2000 respectively.

He is currently with NASA Goddard Space Flight Center, Greenbelt, MD, USA. Prior to this, he was with USDA Agricultural Research Service, Hydrology and Remote Sensing Laboratory, Beltsville, MD, USA. His research interests involve the application of microwave remote sensing in hydrology. He is currently working on soil moisture estimation from microwave sensors and their subsequent application in land surface hydrology.

Dr. Bindlish is a member of American Geophysical Union. He is also a science team member of SMAP, NISAR, Aquarius, and GCOM-W missions.

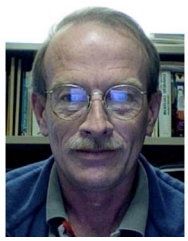

R. Scott Dunbar received the B.S. degree in physics and astronomy from the University of Albany, Albany, NY, USA, in 1976 and the Ph.D. degree in physics from Princeton University, Princeton NJ, USA, in 1980.

He has been with the Jet Propulsion Laboratory, Pasadena, CA, USA, since 1981. Over the last 35 years, he has contributed to the development of science algorithms for the NSCAT and SeaWinds ocean vector wind scatterometer projects, and since 2009, he has been working on SMAP soil moisture and freeze-thaw algorithm development.

Dara Entekhabi (Fellow, IEEE) received the B.S. degree in 1983 and the M.S. degrees in 1985 and 1988 from Clark University, Worcester, MA, USA, both in geography and the Ph.D. degree in civil and environmental engineering from the Massachusetts Institute of Technology (MIT), Cambridge, MA, USA, 1990.

He is currently a Professor with the Department of Civil and Environmental Engineering and the Department of Earth, Atmospheric and Planetary Sciences, MIT. He is also the Science Team lead for the National Aeronautics and Space Administration's Soil Moisture Active and Passive (SMAP) mission that was launched 31 January 2015. His research includes terrestrial remote sensing, data assimilation, and coupled land–atmosphere systems modeling.

Prof. Entekhabi is also a Fellow of the American Meteorological Society and the American Geophysical Union. He is a member of the National Academy of Engineering.

Jun Asanuma received the B.Eng. and M.Eng. degrees in civil engineering from the University of Tokyo, Tokyo, Japan, in 1989 and 1991, respectively, and the Ph.D. degree in civil and environmental engineering from Cornell University, Ithaca, NY, USA, in 1996.

After he was with the Central Research Center of Nippon Koei Company Ltd., Tokyo, Japan, as a Research Engineer in Hydrology, he joined Department of Civil and Environmental Engineering, Nagaoka University of Technology, Nagaoka, Japan. He moved to Terrestrial Environmental Research Center, University of Tsukuba, Tsukuba, Japan, as a Lecturer in 2000. His research interests include land surface hydrology, with emphases on the exchange of mass and energy between the land and the atmosphere through turbulence theories, modeling techniques, and field measurement techniques.

Aaron A. Berg received the B.Sc. and M.Sc. degrees in geography from the University of Lethbridge, Lethbridge, AB, Canada, 1995 and 1997, respectively, and the M.S. degree in geological sciences from the University of Texas at Austin, Austin, TX, USA, in 2001, and the Ph.D. degree in earth system science from the University of California at Irvine, Irvine, CA, USA, in 2003.

Since 2003, he has been with the Department of Geography, Environment and Geomatics, University of Guelph, Guelph, ON, Canada. He teaches in physical geography, hydrology and remote sensing with research interests focused on the modeling and observation of soil moisture.

Alisa Coffin received the the Ph.D. degree in geography from the University of Florida, Gainesville, FL, USA, in 2009.

She is currently a Research Physical Scientist with the USDA—Agricultural Research Service, Tifton, GA, USA. He is also the Research Leader for the Southeast Watershed Research Laboratory. His research focuses on remote and proximal sensing applications relating agricultural land uses and production with water availability and ecosystem services.

Michael H. Cosh (Senior_Member, IEEE) received the Ph.D. degree in civil and environmental engineering from Cornell University, Ithaca, NY, USA, in 2002.

He is currently the Research Leader of the U.S. Department of Agriculture, Agricultural Research Service, Hydrology and Remote Sensing Laboratory, Beltsville, MD, USA. His current research interests include the monitoring of soil moisture from both in situ resources and satellite products.

Dr. Cosh is currently a Fellow of the American Society of Agronomy and the Soil Science Society of America.

Gerald Flerchinger is currently a Retired Research Civil Engineer from the USDA—Agricultural Research Service, Boise, ID, USA. His research focuses on measurement and modeling of surface fluxes to quantify the role of vegetation ecosystems in modulating surface fluxes, microclimate and hydrology. Research interests include the effects of prescribed fire and vegetation management on hydrology, surface fluxes, and ecosystem services.

Ann-Marie Fortuna is currently a Research Soil Scientist with the Agroclimate and Hydraulics Research Unit of the Oklahoma El Reno, OK, USA, and Central Plains Agriculture Research Center, USDA, ARS, El Reno, OK, USA. She works to develop and deliver improved technologies, management strategies, and planning tools to evaluate and manage natural resource concerns and environmental risks, opportunities, and tradeoffs, for integrated systems under variable conditions. Her research integrates knowledge of soil biology, and nutrient cycling into integrated forage-cropping-grazing systems that utilize nutrients and water resources efficiently.

Chandra Holifield Collins received the Doctorate degree in soil, water, and environmental science from the University of Arizona, Tucson, AZ, USA, in 2006.

She is currently a Soil Scientist with the USDA-Agricultural Research Service's Southwest Watershed Research Center, Washington, DC, USA. Her research interests include image analysis and the use of remote sensing data for agricultural applications, with current focus on operational tools for rangeland management.

Taras Lychuk received the B.Sc. degree in environmental engineering and the M.Sc. degree in agricultural sciences from the Ukrainian University of Nature Conservation, Kyiv, Ukraine, 1999 and 2007, respectively, and the Ph.D. degree in soil science and watershed management from the University of Maryland, College Park, MD, USA, 2014.

He is currently a Soil Scientist with Agriculture and Agri-Food Canada's Brandon Research and Development Centre (BRDC). His research at BRDC focuses on soil quality, precision agriculture, nutrient management, crop and soil models, remote sensing and cropping systems, and assessment of climate change impacts on crop production and environmental footprint.

José Martínez-Fernández received the B.S. degree in physical geography, the M.S. degree in water science and technology, and Ph.D. degree in physical geography from the from the Universidad de Murcia (UM), Murcia, Spain, in 1985, 1991, and 1992, respectively.

He was a Research Fellowship (1988–1992) and Junior Researcher (1992–1994) with the Department of Geography, UM. He was an Assistant Professor (1995) and an Associate Professor (1997) with the Department of Geography, Universidad de Salamanca (USAL), Salamanca, Spain, where he has been a Professor of Physical Geography since May 2018. He is also the Principal Investigator (PI) of the Water Resources Research Group, Institute for Agribiotechnology Research (CIALE), USAL. He is author or coauthor of 234 publications.

Dr. Martínez-Fernández has been a PI in 25 national and international (Regional and Spanish Research Programmes, European Union, European Space Agency) research projects and collaborator in 12 research projects. He has been a member of the Spanish National Biodiversity, Earth Sciences and Global Change Programme R&D Projects Selection Committee, and of the Earth and Water Sciences Commission, Spanish Research Agency. He was the recipient of the B.S. degree award.

Kayla Moore received the Ph.D. degree in civil engineering from the University of Manitoba, Winnipeg, Canada, in 2020.

She is currently a Research Scientist with Agriculture and Agri-Food Canada, Brandon, MB, Canada. She leads a program in agro-hydrology. Her research focuses on soil water and groundwater best management practices for agriculture including managing water extremes, sustainable water management, and nutrient fluxes. She is one of the scientists leading the RISMA soil monitoring network.

Zhongbo (Bob) Su received the M.Sc. degree in hydrological engineering from IHE Delft Institute for Water Education, Delft, The Netherlands, and the Ph.D. degree in civil engineering from Ruhr University, Bochum, Germany, 1989 and 1996, respectively.

He is currently an internationally recognized expert in spatial hydrology, Earth observation, and land-atmosphere interactions with 30+ years' experience with the University of Twente, Enschede, The Netherlands. He holds the chair of Spatial Hydrology and Water Resources Management, previously leading UT's Water Resources Department for 15 years. He has held leadership roles at initiatives by ESA, GEO, EGU, and WCRP/GEWEX, advising major satellite missions (e.g., ROSE-L) and steering global hydrology initiatives. He pioneered capacity-building programs (e.g., ESA Dragon/TIGER), supervised 37+ Ph.D.s, and led 54 funded projects. His work advances digital twin earth and soil-plant-atmosphere continuum modeling. His research integrates water–energy–carbon processes using remote sensing, modeling, and machine learning for climate/ecosystem applications.

Jeffrey Walker received the Bachelor of Engineer (Civil) (Hons 1) and Bachelor of Surveying (Hons 1) degrees and the Ph.D. degree in water resources engineering from the University of Newcastle, Callaghan, NSW, Australia, in 1995 and 1999, respectively.

His Ph.D. thesis was among the early pioneering research on estimation of root-zone soil moisture from assimilation of remotely sensed surface soil moisture observations. He then joined NASA Goddard Space Flight Centre to implement his soil moisture work globally. In 2001, he moved to the Department of Civil and Environmental Engineering, University of Melbourne, Parkville, VIC, as a Lecturer, where he continued his soil moisture work, including development of the only Australian airborne capability for simulating new satellite missions for soil moisture. In 2010, he was appointed as a Professor with the Department of Civil Engineering, Monash University, Clayton VIC, Australia, where he is continuing this research.

Dr. Walker is contributing to soil moisture satellite missions at NASA, ESA and JAXA, as a Science Team member for the Soil Moisture Active Passive (SMAP) mission and Cal/val Team member for the Soil Moisture and Ocean Salinity (SMOS) and Global Change Observation Mission – Water (GCOM-W) respectively. He was the recipient of the University Medal from the University of Newcastle.